

**Synthesis and electrochemistry of  $(\text{CO})_2(\text{PMe}_3)\text{Fe}(\mu\text{-}2\text{-tert-Bu}_2\text{P})(\mu\text{-}2\text{-CO})\text{Rh}(\text{PMe}_3)\text{L}(\text{Fe-Rh})$  (L = CO,  $\text{PMe}_3$ ). Digital simulation of modified ECE mechanism. X-ray crystal structures of  $(\text{CO})_2(\text{PMe}_3)\text{Fe}(\mu\text{-}2\text{-tert-Bu}_2\text{P})(\mu\text{-}2\text{-CO})\text{Rh}(\text{PMe}_3)_2$  and  $[\text{Me}_3\text{PO}\cdot\text{Na}(15\text{-crown-}5)]^+[(\text{CO})_3\text{Fe}(\mu\text{-}2\text{-tert-Bu}_2\text{P})\text{Rh}(\text{PMe}_3)(\text{CO})]^-$**

Roger D. Moulton, Don J. Chandler, Atta M. Arif, Richard A. Jones, and Allen J. Bard

*J. Am. Chem. Soc.*, **1988**, 110 (17), 5714-5725 • DOI: 10.1021/ja00225a023

Downloaded from <http://pubs.acs.org> on February 2, 2009

### More About This Article

---

The permalink <http://dx.doi.org/10.1021/ja00225a023> provides access to:

- Links to articles and content related to this article
- Copyright permission to reproduce figures and/or text from this article



**ACS Publications**  
High quality. High impact.

5. The europium ion fluorescence is effectively quenched by molecular oxygen following Stern-Volmer kinetics.

**Acknowledgment.** The generous financial assistance of the Natural Science and Engineering Research Council of Canada's Operating and Strategic Grants Programmes and the Connaught

Foundation of the University of Toronto is greatly appreciated. We are also indebted to Dr. Edith Flanigen (Union Carbide) for supplying various high-crystallinity and ultrahigh-purity FAU zeolites as well as invaluable technical discussions.

**Registry No.** Eu<sup>3+</sup>, 22541-18-0; EuCl<sub>3</sub>, 10025-76-0; O<sub>2</sub>, 7782-44-7.

## Synthesis and Electrochemistry of (CO)<sub>2</sub>(PMe<sub>3</sub>)Fe(μ<sub>2</sub>-*t*-Bu<sub>2</sub>P)(μ<sub>2</sub>-CO)Rh(PMe<sub>3</sub>)L(*Fe-Rh*) (L = CO, PMe<sub>3</sub>). Digital Simulation of Modified ECE Mechanism. X-ray Crystal Structures of (CO)<sub>2</sub>(PMe<sub>3</sub>)Fe(μ<sub>2</sub>-*t*-Bu<sub>2</sub>P)(μ<sub>2</sub>-CO)Rh(PMe<sub>3</sub>)<sub>2</sub> and [Me<sub>3</sub>PO·Na(15-crown-5)]<sup>+</sup>[(CO)<sub>3</sub>Fe(μ<sub>2</sub>-*t*-Bu<sub>2</sub>P)Rh(PMe<sub>3</sub>)- (CO)]<sup>-</sup>

Roger D. Moulton, Don J. Chandler, Atta M. Arif, Richard A. Jones,\* and Allen J. Bard\*

Contribution from the Department of Chemistry, The University of Texas at Austin, Austin, Texas 78712. Received August 14, 1987

**Abstract:** Reaction of the lithiated iron phosphine complex Fe(CO)<sub>3</sub>(*t*-Bu<sub>2</sub>PH)(*t*-Bu<sub>2</sub>PLi) with (Rh(CO)<sub>2</sub>Cl)<sub>2</sub> or Rh(PMe<sub>3</sub>)<sub>3</sub>Cl in THF yields the heterobimetallic phosphido bridged complexes (CO)<sub>3</sub>(*t*-Bu<sub>2</sub>PH)Fe(μ<sub>2</sub>-*t*-Bu<sub>2</sub>P)Rh(CO)<sub>2</sub> (**1**) and (CO)<sub>2</sub>(PMe<sub>3</sub>)Fe(μ<sub>2</sub>-*t*-Bu<sub>2</sub>P)(μ<sub>2</sub>-CO)Rh(PMe<sub>3</sub>)<sub>2</sub> (**2**), respectively. **2** can also be prepared from (CO)<sub>2</sub>(*t*-Bu<sub>2</sub>PH)Fe(μ<sub>2</sub>-*t*-Bu<sub>2</sub>P)(μ<sub>2</sub>-CO)Rh(COD) and excess PMe<sub>3</sub> (COD = 1,5-cyclooctadiene). Reaction of **1** with PMe<sub>3</sub> or **2** with CO (1 atm) yields (CO)<sub>3</sub>(PMe<sub>3</sub>)Fe(μ<sub>2</sub>-*t*-Bu<sub>2</sub>P)Rh(CO)(PMe<sub>3</sub>) (**3**). Both **2** and **3** may be reduced with Na sand to radical anions, and the reduction of **3** in the presence of 15-crown-5 and traces of O<sub>2</sub> led to the isolation of [(15-crown-5)Na(Me<sub>3</sub>P=O)]<sup>+</sup>[(CO)<sub>3</sub>Fe(μ<sub>2</sub>-*t*-Bu<sub>2</sub>P)Rh(CO)(PMe<sub>3</sub>)]<sup>-</sup> (**4**). The molecular structures of **2** and **4** have been determined via single-crystal X-ray diffraction studies. The molecular geometries of both complexes contain a di-*tert*-butylphosphido unit which spans a single Fe-Rh bond. In **2** the Fe atom is six coordinate if one includes the Fe-Rh bond. If one excludes the Fe-Rh bond the geometry about Fe may be considered to be trigonal bipyramidal. The Rh atom in **2** is five coordinate, including the Fe-Rh bond. The geometry about Rh is best described as a square-based pyramid with the carbon atom of the bridging CO unit occupying the vertex. In **4** the coordination geometry about Fe is trigonal bipyramidal and about Rh it is roughly square planar including the Fe-Rh bond in both cases. The molecular geometry of **3** is similar to that of **2** based on spectroscopic evidence. Cyclic voltammetry of **2** and **3** shows two oxidation waves and an irreversible two-electron reduction wave. The product of the reduction is oxidized in a reversible 1 e<sup>-</sup> process to an anion radical that can be further oxidized to reform the original compound. A third oxidation at low scan rates or at high concentrations is also seen. Digital simulations of the voltammetry show this wave corresponds to a dianion species formed by a disproportionation reaction in solution. Possible structures of the electrochemically produced species are proposed. X-ray crystal data for **2** (C<sub>20</sub>H<sub>45</sub>FeO<sub>3</sub>P<sub>4</sub>Rh): *M* = 616.23, monoclinic, *P*2<sub>1</sub>, (No. 4), *a* = 10.719 (2) Å, *b* = 10.148 (3) Å, *c* = 13.637 (3) Å, β = 95.63 (2)°, *U* = 1476.1 (5) Å<sup>3</sup>, *D*<sub>c</sub> = 1.386 g cm<sup>-3</sup>, *Z* = 2, μ(Mo Kα) = 12.72 cm<sup>-1</sup>. Refinement of 1756 reflections (*I* > 3σ(*I*)) out of 2756 unique observed reflections (2° < 2θ < 50°) gave *R* and *R*<sub>w</sub> values of 0.054 and 0.059, respectively. Crystal data for **4** (C<sub>28</sub>H<sub>56</sub>FeNaO<sub>10</sub>P<sub>3</sub>Rh): *M* = 826.97, monoclinic, *P*2<sub>1</sub>/c, (No. 14), *a* = 12.246 (3) Å, *b* = 10.688 (5) Å, *c* = 31.326 (5) Å, β = 94.63 (2)°, *U* = 4087.0 (5) Å<sup>3</sup>, *D*<sub>c</sub> = 1.142 g cm<sup>-3</sup>, *Z* = 4, μ(Mo Kα) = 9.17 cm<sup>-1</sup>. Refinement of 1670 unique observed reflections (3° < 2θ < 48°) gave *R* and *R*<sub>w</sub> values of 0.087 and 0.096, respectively. Common to both structures: λ(Mo Kα) = 0.71073 Å, graphite monochromator. MULTAN, difference Fourier, and full-matrix least squares were the methods used.

Electrochemical investigations of bimetallic organometallic complexes often demonstrate that conformational changes and isomerizations occur prior to and following electron transfer.<sup>1</sup> Electrochemistry thus serves as a probe into the reactivity and stability of complexes in new oxidation states. For example, electrochemistry has been applied to the study of the effect of the electron transfer on the metal-metal interaction.<sup>2</sup> Reduction of a dinuclear species tends to decrease the metal-metal bond order, whereas oxidation tends to increase it. If the metal-metal bond is disrupted following electron transfer, the presence of a bridging

group may help to maintain the integrity of the complex. Geometric isomerization or bonding rearrangements in the coordination sphere may also occur following reduction or oxidation, especially with complexes in which bonds are strained. Thus, there has been considerable interest in the study of reactions that accompany electron transfer, and the effect these have on the observed electrochemistry.

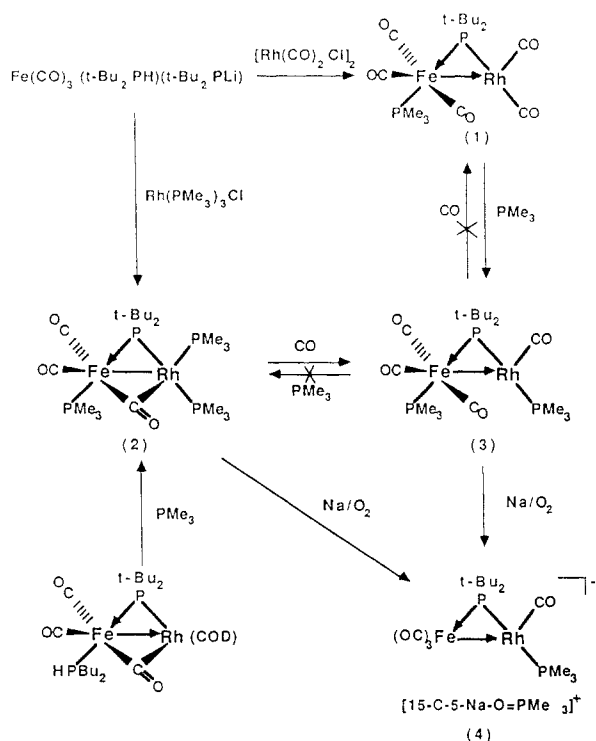
We have been investigating the effect of structure of bimetallic systems on homogeneous reactivity<sup>3</sup> and on the redox processes

(1) (a) Kotz, J. C. In *Topics in Organic Electrochemistry*; Fry, A. J., Britton, W. E., Eds.; Plenum: New York, 1986; p 83 and references therein. (b) Evans, D. H.; O'Connell, K. M. In *Electroanalytical Chemistry*; Bard, A. J., Ed.; Marcel Dekker: New York, 1986; Vol. 14, p 113.

(2) Roberts, D. A.; Geoffroy, G. L. *Comprehensive Organometallic Chemistry*; Wilkinson, G., Stone, F. G. A., Abel, E. W., Eds.; Pergamon: New York, 1982; Vol. 6, Chapter 40.

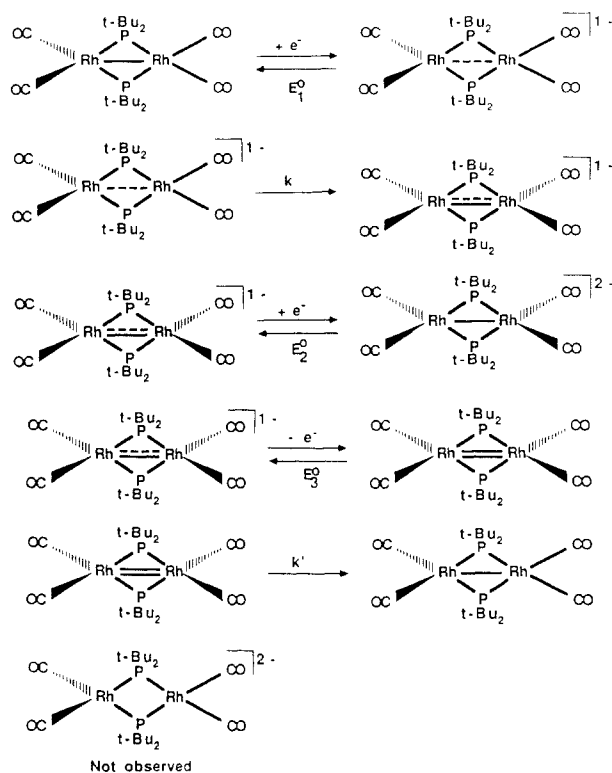
(3) (a) Chandler, D. J.; Jones, R. A.; Stuart, A. L.; Wright, T. C. *Organometallics* **1984**, 3, 1830. (b) Jones, R. A.; Wright, T. C. *Organometallics* **1983**, 2, 1842. (c) Atta, A. M.; Chandler, D. J.; Jones, R. A. *Organometallics* **1987**, 6, 506. (d) Chandler, D. J. Ph.D. dissertation, The University of Texas, 1986, and references therein. (e) Arif, A. M.; Heaton, D. E.; Jones, R. A.; Kidd, K. B.; Wright, T. C.; Whittlesey, B. R.; Atwood, J. L.; Hunter, W. E.; Zhang, H. *Inorg. Chem.* **1987**, 26, 4065.

Scheme I



observed.<sup>4,5</sup> These studies have included the competing steric and electronic effects associated with the bridging di-*tert*-butylphosphido ( $t\text{-Bu}_2\text{P}^*$ ) group. For example, we recently reported details of the synthesis<sup>6</sup> and electrochemistry<sup>4</sup> of the dinuclear phosphido-bridged system based on  $[\text{Rh}(\mu_2\text{-}t\text{-Bu}_2\text{P})(\text{CO})_2]_2$ . In the course of studying other phosphido-bridged systems, we were able to isolate and characterize a series of Fe-Rh heterobimetallic complexes as shown in Scheme I.<sup>3c</sup> The complexes are similar to  $[\text{Rh}(\mu_2\text{-}t\text{-Bu}_2\text{P})(\text{CO})_2]_2$  in that they contain a Rh atom bonded both directly and via a bridge to a second metal. However, for **2** the five-coordinate Rh atom in the neutral complex has geometry best described as a square-based pyramid with the carbon atom of a bridging CO unit occupying the vertex.

Electrochemical studies on  $[\text{Rh}(\mu_2\text{-}t\text{-Bu}_2\text{P})(\text{CO})_2]_2$  show that the molecule undergoes an ECE-DISP1<sup>7,8</sup> process upon reduction<sup>4</sup> and an EEC process upon oxidation (Scheme II). The chemical reaction coupled to the reduction processes is the interconversion of isomers that have square-planar and tetrahedral rhodium atoms in the anion radical. In previous studies<sup>7,9</sup> of the ECE mechanism, the voltammetric response has been shown to be strongly affected by the value of the equilibrium constant for the intervening chemical reaction. This equilibrium constant is frequently found to be large in organometallic systems because bond strain in the new oxidation state may cause the molecule to relax to a more stable conformation. When the relaxation process is irreversible, two individual  $1e^-$  transfers may be observed as the electrode returns to the starting potential, since the irreversibility of the relaxation prevents a concerted  $2e^-$  process from occurring.<sup>10</sup> The

Scheme II. ECE/EEC Electrochemical Mechanism for  $[\text{Rh}(\mu_2\text{-}t\text{-Bu}_2\text{P})(\text{CO})_2]_2$ 

ECE/EEC mechanism provides access to five electroactive species during the voltammetry cycle (see Scheme II). One species is missing in Scheme II: a compound in the oxidation state of the product of the ECE process, but whose structure matches that of the starting material. This species can be formed by disproportionation of one of the intermediates in the mechanism (the "ECE-DISP3" case<sup>9</sup>), but examples of organometallic complexes displaying this effect are rare. In this paper, we present an example of a different DISP process coupled with the ECE/EEC mechanism which provides access to all six possible isomers and oxidation states.

The sequence of the electrochemical and chemical reactions (if any) in a mechanism is central to all studies of organic and organometallic electrochemistry.<sup>11</sup> No general strategy for determining an electrochemical mechanism has been developed. The behavior of many simple mechanisms has been described.<sup>12</sup> However, often the electrode mechanism is more complex, and a computer simulation of the electrochemical experiment may be necessary to verify that a proposed mechanism is consistent with the observed electrochemical behavior. A successful simulation requires close agreement with the observed voltammetry under a variety of experimental conditions (concentration, scan rate, pH, etc.) and provides the values of the rate constants for the chemical and heterogeneous electron-transfer steps in the mechanism. For example, digital simulations of the ECE-DISP1 case have been used to estimate<sup>4</sup> the value of the second-order rate constants from repeated sweeps in a cyclic voltammetric experiment. In our studies of complexes **2** and **3**, the effect of changes in the voltammetric sweep rate, switching potential, concentration, and the CV behavior on subsequent sweeps were used to obtain the

(4) Gaudiello, J. G.; Wright, T. C.; Jones, R. A.; Bard, A. J. *J. Am. Chem. Soc.* **1985**, *107*, 888.

(5) (a) Moulton, R. D.; Weidman, T. W.; Vollhardt, K. P. C.; Bard, A. J. *Inorg. Chem.* **1986**, *25*, 1846. (b) Bligh, R. Q.; Moulton, R. D.; Bard, A. J.; Piorka, A.; Sutherland, R. G. *Inorg. Chem.*, submitted for publication. (c) Moulton, R. D.; Bard, A. J. *Organometallics* **1988**, *7*, 351.

(6) Jones, R. A.; Wright, T. C.; Atwood, J. L.; Hunter, W. E. *Organometallics* **1983**, *2*, 470.

(7) Nadjo, L.; Saveant, J. M. *J. Electroanal. Chem.* **1973**, *48*, 113.

(8) (a) Hawley, D. M.; Feldberg, S. W. *J. Phys. Chem.* **1966**, *70*, 3459. (b) Adams, R. N.; Hawley, M. D.; Feldberg, S. W. *J. Phys. Chem.* **1967**, *71*, 851. (c) Feldberg, S. W. *J. Phys. Chem.* **1971**, *75*, 2377. (d) Feldberg, S. W.; Jetic, L. *J. Phys. Chem.* **1972**, *76*, 2439.

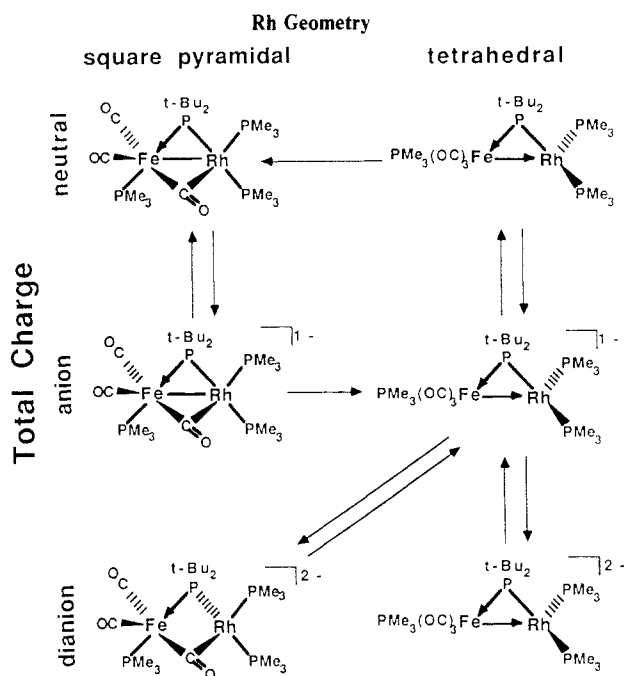
(9) Amatore, C.; Gareil, M.; Saveant, J. M. *J. Electroanal. Chem.* **1983**, *147*, 1 and references therein.

(10) See, for example: (a) Dietrich, M.; Heinze, J.; Fischer, H.; Neugebauer, F. *Angew. Chem., Int. Ed. Engl.* **1986**, *25*, 1021. (b) Hinkelmann, K.; Mahlendorf, F.; Heinze, J.; Schacht, H.-T.; Field, J. S.; Vahrenkamp, H. *Angew. Chem., Int. Ed. Engl.* **1987**, *26*, 352.

(11) Hawley, M. D. In *Laboratory Techniques in Electroanalytical Chemistry*; Kissinger, P. T., Heineman, W. R., Eds.; Marcel Dekker: New York, 1984; p 463.

(12) (a) Hanafey, M. K.; Scott, R. L.; Ridgway, T. H.; Reilley, C. N. *Anal. Chem.* **1978**, *50*, 116. (b) Andrieux, C. P.; Saveant, J. M. In *Investigations of Rates and Mechanisms of Reactions*; Bernasconi, C. F., Ed.; Wiley: New York, 1986; Vol. 6, 4/E, Part 2.

Scheme III



stoichiometry and rate constants for two homogeneous reactions coupled to an ECE mechanism. We believe this method is of general utility for studies that explore the reactivity of intermediates in an electrochemical mechanism.

### Results and Discussion

**Synthesis of Neutral Fe–Rh Complexes: 1, 2, and 3.** Nucleophilic attack of a lithiated iron phosphine complex (in this case  $\text{Fe}(\text{CO})_3(\text{t-Bu}_2\text{PH})(\text{t-Bu}_2\text{PLi})$ ) on Rh chloride complexes has been studied as a methodology for the formation of Fe–Rh bonds.<sup>13</sup> By this method, we were able to generate in moderate yield  $(\text{CO})_3(\text{t-Bu}_2\text{PH})\text{Fe}(\mu_2\text{-t-Bu}_2\text{P})\text{Rh}(\text{CO})_2$  (**1**) by using  $[\text{Rh}(\text{CO})_2\text{Cl}]_2$ , and  $(\text{CO})_2(\text{PMe}_3)\text{Fe}(\mu_2\text{-t-Bu}_2\text{P})(\mu_2\text{-CO})\text{Rh}(\text{PMe}_3)_2$  (**2**) with  $\text{Rh}(\text{PMe}_3)_3\text{Cl}$ . Scheme I shows the new compounds and Schemes II and III the species we believe are responsible for the electrochemical behavior in  $[\text{Rh}(\mu_2\text{-t-Bu}_2\text{P})(\text{CO})_2]_2$  and in this study, respectively. It should be noted that we have depicted the bonding of the  $\mu_2\text{-t-Bu}_2\text{P}$  group and the Fe–Rh bond in some cases as involving dative  $\text{P} \rightarrow \text{Fe}$  and  $\text{Fe} \rightarrow \text{Rh}$  bonds. We emphasize that this is merely to assist in the formal electron counting in these species. It is well recognized that the assignment of formal oxidation states and electron counts is frequently ambiguous. Nevertheless, by using the notation shown, the formal electron counts for the species shown in Scheme III are all reasonable. Complex **2** is also available from  $(\text{CO})_2(\text{t-Bu}_2\text{PH})\text{Fe}(\mu_2\text{-t-Bu}_2\text{P})(\mu_2\text{-CO})\text{Rh}(\text{COD})^{3c}$  and excess  $\text{PMe}_3$ . The complexes **1** and **2** can be converted in high yield to  $(\text{CO})_3(\text{PMe}_3)\text{Fe}(\mu_2\text{-t-Bu}_2\text{P})\text{Rh}(\text{CO})(\text{PMe}_3)$  (**3**) by a reaction with  $\text{PMe}_3$  and  $\text{CO}$ , respectively. In contrast, we discovered that **3** is unreactive with  $\text{CO}$  or  $\text{PMe}_3$ . NMR data for **1–3** support the overall proposed geometries as shown in Scheme I. Thus, NMR coupling constants between the phosphorus atoms suggest the Rh– $\text{PMe}_3$  bond in **3** is trans to the bridging phosphido group. In addition to phosphine resonances, the  $^{31}\text{P}\{^1\text{H}\}$  NMR spectra show downfield multiplets assigned to the phosphido groups which bridge a metal–metal bond.<sup>14</sup> Infrared data suggest that only **2** and  $(\text{CO})_2(\text{t-Bu}_2\text{PH})\text{Fe}(\mu_2\text{-t-Bu}_2\text{P})(\mu_2\text{-CO})\text{Rh}(\text{COD})$  have bridging CO groups

(13) Breen, M. J.; Duttera, M. R.; Geoffroy, G. L.; Novotnak, G. C.; Roberts, D. A.; Shulman, P. M.; Steinmetz, G. R. *Organometallics* **1982**, *1*, 1008.

(14) Downfield shifts in the  $\delta$  50–200 range in the  $^{31}\text{P}$  NMR of the  $\text{Ph}_2\text{P}$  groups bridging metal–metal bonds have been noted by several groups of workers. See, for example: Garrou, P. E. *Chem. Rev.* **1981**, *81*, 229. Carty, A. J. *Adv. Chem. Ser.* **1982**, No. 196, 163 and references 1–5 therein. Similar downfield shifts have been noted for  $\mu_2\text{-t-Bu}_2\text{P}$  complexes: see ref 3c, 4, and 6.

Table I. Crystal Structure Parameters for Complexes **2** and **4**

	<b>2</b>	<b>4</b>
Description of Crystal		
color	orange	yellow
habit	plate	plate
max crystal dimens (mm)	0.30 × 0.25 × 0.25	0.20 × 0.15 × 0.10
Unit Cell		
crystal system	monoclinic	monoclinic
space group	$P2_1$	$P2_1/c$
unit cell params		
<i>a</i> (Å)	10.719 (2)	12.246 (3)
<i>b</i> (Å)	10.148 (3)	10.688 (5)
<i>c</i> (Å)	13.637 (3)	31.326 (5)
$\alpha$ (deg)	90	90
$\beta$ (deg)	95.63 (2)	94.63 (2)
$\gamma$ (deg)	90	90
<i>U</i> (Å <sup>3</sup> )	1476.1 (5)	4087.0 (5)
<i>Z</i>	2	4
formula	$\text{C}_{20}\text{H}_{45}\text{FeO}_3\text{P}_4\text{Rh}$	$\text{C}_{28}\text{H}_{56}\text{FeNaO}_{16}\text{P}_3\text{Rh}$
mol wt (g·mol <sup>-1</sup> )	616.23	826.97
calcd density (g·cm <sup>-3</sup> )	1.38	1.142
$\mu$ -calcd (cm <sup>-1</sup> )	12.72	9.17
Data Collection		
radiation (Å)	Mo K $\alpha$ (0.71073)	Mo K $\alpha$ (0.71073)
scan technique	$\theta/2\theta$	$\theta/2\theta$
scan width (deg)	0.8 + 0.35(tan $\theta$ )	0.8 + 0.35(tan $\theta$ )
range of indices ( <i>h,k,l</i> )	$\pm 12, +12, +16$	$+13, +11, \pm 32$
$2\theta$ range (deg)	2 to 50	3 to 48
no. of reflns measured	2756	6831
standard reflns:		
intensity	613, 227	248, $\bar{6}$ 12
orientation	317, 612	5210, $\bar{2}$ 49
decay of stds (%)	3	25
min % transmission	78.31	
max % transmission	99.89	
av % transmission	94.21	
agreement factor for averaged reflns		
<i>F</i> (obsd)	0.045	0.031
intensity	0.040	0.040
Structure Determination		
no. of reflns used ( <i>I</i> > 3 $\sigma$ ( <i>I</i> ))	1756	1670
no. of params varied	207	207
data/param ratio	8.483	8.068
shift to error ratio	2.520	0.264
esd of an observation of unit wt	4.39	3.83
<i>R</i>	0.0540	0.0870
<i>R</i> <sub>w</sub>	0.0590	0.0960

Table II. Selected Bond Lengths (Å) for **2**<sup>a</sup>

atom 1	atom 2	distance	atom 1	atom 2	distance
Rh	Fe	2.665 (1)	P2	C5	1.89 (2)
Rh	P1	2.279 (2)	P2	C6	1.81 (2)
Rh	P3	2.326 (3)	P3	C15	1.850 (15)
Rh	P4	2.249 (3)	P3	C16	1.75 (2)
Rh	C1	2.177 (9)	P3	C17	1.845 (15)
Fe	P1	2.267 (3)	P4	C18	1.78 (2)
Fe	P2	2.209 (3)	P4	C19	1.80 (2)
Fe	C1	1.840 (10)	P4	C20	1.79 (2)
Fe	C2	1.737 (12)	O1	C1	1.190 (11)
Fe	C3	1.805 (15)	O2	C2	1.172 (12)
P1	C7	1.944 (10)	O3	C3	1.12 (2)
P1	C11	1.918 (9)			
P2	C4	1.814 (15)			

<sup>a</sup>Numbers in parentheses are estimated standard deviations in the least significant digits.

( $\nu_{\text{CO}} = 1735 \text{ cm}^{-1}$  (mbr. for **2**), and this is observed in the solid-state X-ray structures.

**X-ray Structure of 2.** Crystals of **2** grow as orange plates in the monoclinic space group  $P2_1$  with two molecules in the unit cell. A view of the molecule is shown in Figure 1. Crystallo-

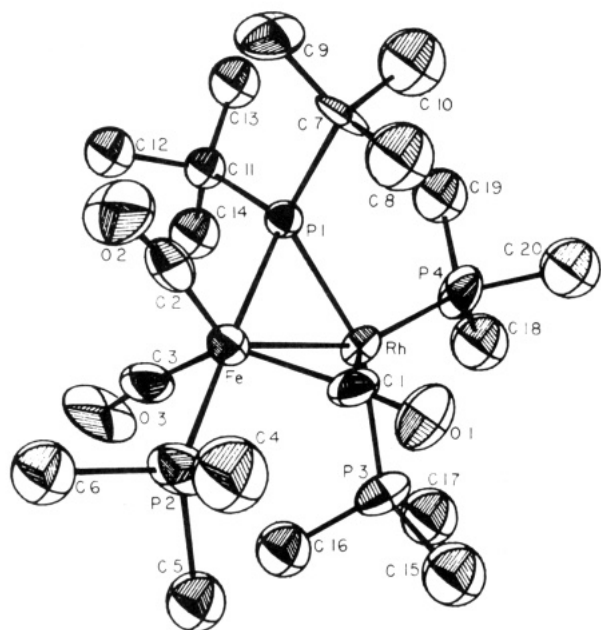


**Figure 1.** ORTEP view of **2** showing the atom numbering scheme. The atoms are shown at the 50% probability level.

**Table III.** Selected Bond Angles (deg) for **2**

atom 1	atom 2	atom 3	angle	atom 1	atom 2	atom 3	angle
Fe	Rh	P1	53.80 (7)	Fe	P1	C11	116.9 (3)
Fe	Rh	P3	105.5 (1)	Fe	P2	C4	116.1 (5)
Fe	Rh	P4	157.8 (1)	Fe	P2	C5	120.4 (5)
Fe	Rh	C1	43.2 (3)	Fe	P2	C6	114.4 (7)
P1	Rh	P3	156.9 (11)	Rh	C1	Fe	82.7 (4)
P1	Rh	P4	104.7 (1)	Rh	C1	O1	122.0 (8)
P1	Rh	C1	81.5 (2)	Fe	C1	O1	155.0 (8)
P3	Rh	P4	96.6 (1)	Fe	C2	O2	173 (1)
P3	Rh	C1	88.8 (3)	Fe	C3	O3	173 (1)
P4	Rh	C1	137.1 (4)	Rh	P3	C15	121.2 (5)
Rh	Fe	P1	54.31 (7)	Rh	P3	C16	111.8 (6)
Rh	Fe	P2	128.4 (1)	Rh	P3	C17	119.1 (5)
Rh	Fe	C1	54.1 (3)	Rh	P4	C18	121.5 (9)
Rh	Fe	C2	140.5 (4)	Rh	P4	C19	120.5 (6)
Rh	Fe	C3	91.7 (5)	Rh	P4	C20	117.9 (7)
P1	Fe	P2	170.6 (2)				
P1	Fe	C1	89.6 (4)				
P1	Fe	C2	89.0 (4)				
P1	Fe	C3	99.3 (4)				
P2	Fe	C1	86.5 (4)				
P2	Fe	C2	85.6 (4)				
P2	Fe	C3	89.8 (4)				
C1	Fe	C2	120.1 (6)				
C1	Fe	C3	129.1 (6)				
C2	Fe	C3	110.2 (6)				
Rh	P1	Fe	71.79 (8)				
Rh	P1	C7	122.6 (4)				
Rh	P1	C11	117.4 (3)				
Fe	P1	C7	115.0 (3)				

graphic data are given in Table I. Key bond lengths and angles are given in Tables II and III, respectively, and positional parameters are given in Table IV. Although the Fe atom is six coordinate, if one excludes the Fe–Rh bond, the geometry about the Fe may be considered to be trigonal bipyramidal. There are

**Table IV.** Positional Parameters for **2**

atom	x	y	z	B (Å <sup>2</sup> ) <sup>a</sup>
Rh	0.9141 (1)	0.2316 (3)	0.7334 (1)	3.53 (2)
Fe	0.7001 (3)	0.175	0.8085 (2)	3.64 (5)
P1	0.7251 (4)	0.3301 (5)	0.6925 (3)	2.99 (9)
P2	0.6717 (7)	0.0511 (8)	0.9377 (5)	7.0 (2)
P3	1.0518 (6)	0.0631 (8)	0.7860 (5)	5.6 (1)
P4	1.0507 (5)	0.3493 (9)	0.6540 (5)	6.1 (2)
O1	0.908 (1)	0.270 (2)	0.9498 (9)	6.7 (5)
O2	0.457 (1)	0.283 (2)	0.841 (1)	8.4 (5)
O3	0.661 (3)	-0.064 (2)	0.689 (2)	11.9 (7)
C1	0.846 (2)	0.231 (3)	0.879 (1)	4.6 (4)
C2	0.558 (2)	0.247 (3)	0.828 (1)	5.5 (5)
C3	0.675 (2)	0.033 (3)	0.730 (2)	6.0 (6)
C4	0.661 (3)	0.138 (3)	1.053 (2)	11.1 (9)
C5	0.779 (3)	-0.093 (4)	0.971 (2)	11.3 (9)*
C6	0.523 (4)	-0.035 (4)	0.929 (3)	14 (1)*
C7	0.689 (2)	0.510 (2)	0.731 (1)	4.5 (5)
C8	0.731 (3)	0.525 (2)	0.838 (2)	8.4 (8)
C9	0.550 (2)	0.548 (3)	0.713 (2)	7.1 (7)
C10	0.764 (3)	0.610 (3)	0.667 (2)	9.6 (9)
C11	0.645 (2)	0.298 (2)	0.563 (1)	3.8 (4)*
C12	0.506 (2)	0.253 (3)	0.572 (1)	5.7 (5)
C13	0.640 (2)	0.415 (3)	0.492 (2)	6.2 (6)*
C14	0.708 (2)	0.184 (3)	0.519 (2)	6.4 (6)*
C15	1.193 (3)	0.029 (3)	0.723 (2)	8.2 (8)*
C16	0.980 (3)	-0.091 (4)	0.775 (2)	10.5 (9)*
C17	1.126 (3)	0.065 (3)	0.914 (2)	8.4 (8)*
C18	1.175 (4)	0.272 (6)	0.598 (3)	20 (2)*
C19	1.000 (4)	0.433 (4)	0.541 (3)	13 (1)*
C20	1.130 (4)	0.484 (5)	0.718 (3)	15 (1)*

<sup>a</sup> Atoms with an asterisk were refined isotropically. Anisotropically refined atoms are given in the form of the isotropic equivalent thermal parameter defined as  $(4/3)[a^2B(1,1) + b^2B(2,2) + c^2B(3,3) + ab(\cos \gamma)B(1,2) + ac(\cos \beta)B(1,3) + bc(\cos \alpha)B(2,3)]$ .

slight deviations from idealized geometries, and these can be accounted for on steric grounds. Thus, the P(1)–Fe–P(2) angle about Fe is 170.6 (2)° and the angles between the CO ligands average 119.8°, which is close to the expected 120°.

The key structural feature of relevance to the electrochemical studies is the coordination geometry about Rh. The Rh atom in **2** is five coordinate (including the Fe–Rh) and its geometry is best described as that of a distorted square-based pyramid with the carbon atom of the bridging CO unit occupying the vertex. Thus, P(3) and P(4) are twisted slightly out of the plane containing Fe, P(1), Rh, P(3), and P(4).<sup>15</sup> The dihedral angle between planes Rh–P(3)–P(4) and Fe–Rh–P(1) is 12.4°. This is an unusual geometry for Rh(I) and we believe it has a significant bearing on our interpretation of the electrochemical results. The important point here is that the coordination about Rh may be easily converted to tetrahedral by removal of (or by ignoring) the Fe–Rh bond or to distorted square planar by detachment of the bridging CO ligand from Rh. In addition, we know that the square-planar Rh atom in  $[\text{Rh}(\mu_2\text{-}t\text{-Bu}_2\text{P})(\text{CO})_2]_2$  isomerizes to tetrahedral upon reduction.<sup>4</sup> Thus, detachment of C(1) from Rh will initially give a distorted square-planar Rh atom that is now free to convert to a tetrahedral form simply by a twist of approximately 90° for the P(4)–Rh–P(3) plane. It is possible that these types of isomerization could accompany the electrochemical reduction and this is described more fully below.

**Chemical Reduction of 2 and 3; Isolation and Characterization of 4.** Reaction of a THF solution of **3** with excess sodium sand results in a rapid color change from yellow to deep red. The <sup>31</sup>P{<sup>1</sup>H} NMR spectrum of this solution shows a doublet of doublets at  $\delta$  270.73. This is assigned to a  $\mu_2\text{-}t\text{-Bu}_2\text{P}$  group, and it is shifted downfield from that observed in **3** ( $\delta$  227.42). The addition of 15-crown-5 to this solution causes the <sup>31</sup>P{<sup>1</sup>H} NMR spectrum to shift only slightly, indicating that the anionic species present in solution is essentially unaffected by the addition of the crown ether.

(15) Deviations (Å) from the least-squares planes are as follows: For **2**: Fe 0.129 (2), Rh -0.004 (2), P(1) 0.199 (5), P(3) 0.251 (7), P(4) -0.307 (8). For **4**: Rh 0.025 (2), Fe 0.030 (4), P(1) -0.049 (7), P(2) -0.031 (8), C(4) 0.03 (3).

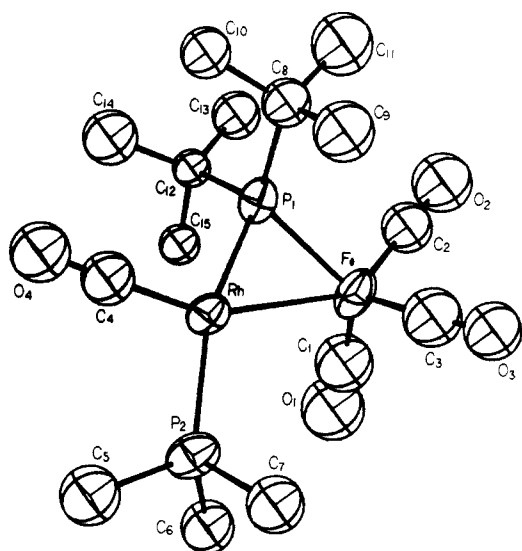


**Figure 2.** ORTEP view of **4** (anion) showing the atom numbering scheme. The atoms are shown at the 50% probability level.

**Table V.** Selected Bond Lengths (Å) for **4**<sup>a</sup>

atom 1	atom 2	distance	atom 1	atom 2	distance
Rh	Fe	2.796 (5)	P3	C28	1.80 (5)
Rh	P1	2.266 (8)	Na1	O5	2.42 (3)
Rh	P2	2.292 (8)	Na1	O6	2.44 (3)
Rh	C4	1.78 (3)	Na1	O7	2.45 (3)
Fe	P1	2.217 (8)	Na1	O8	2.40 (3)
Fe	C1	1.69 (3)	Na1	O9	2.43 (3)
Fe	C2	1.69 (3)	Na1	O10	2.13 (3)
Fe	C3	1.68 (4)			
P1	C8	1.89 (3)			
P1	C12	1.98 (3)			
P2	C5	1.79 (4)			
P2	C6	1.85 (3)			
P2	C7	1.89 (3)			
P3	O10	1.48 (3)			
P3	C26	1.81 (5)			
P3	C27	1.79 (4)			

<sup>a</sup>Numbers in parentheses are estimated standard deviations in the least significant digits.

If the reduction is performed under rigorously anaerobic conditions, the product is isolated as a red oil, and we have been unable to isolate crystals suitable for X-ray analysis from the reduced solutions. However, the addition of small amounts of oxygen permits the isolation of the radical anion  $[(\text{CO})_3\text{Fe}(\mu_2\text{-}t\text{-Bu}_2\text{P})\text{Rh}(\text{CO})(\text{PMe}_3)]^-$  with the unusual counteranion  $[\text{Me}_3\text{PO}\cdot\text{Na}(15\text{-crown-5})]^+$  (**4**).  $^{31}\text{P}\{^1\text{H}\}$  NMR spectra for the reduced solutions, before and after addition of 15-crown-5 and oxygen, are virtually identical with those of isolated **4**. Similarly, the room temperature ESR spectrum of **4** (which shows a broad signal at  $g = 2.074$ ) is identical with the crude reaction mixture (either in the presence or absence of the crown ether or  $\text{O}_2$ ). These observations are consistent with the chemical reduction of **3** generating the anion radical **4**. The presence of  $\text{O}_2$  serves to oxidize the  $\text{PMe}_3$  to the phosphine oxide  $\text{Me}_3\text{P}=\text{O}$ , which is apparently necessary for the formation of crystals suitable for X-ray crystallography, and it does not affect the structure or oxidation state of the organometallic fragment formed during the reduction. We were not able to inhibit the release of  $\text{PMe}_3$  which accompanies the reduction, and no other species was isolated, even when the reduction was performed at  $-78^\circ\text{C}$  with  $\text{PMe}_3$  added to the solution.

**X-ray Structure of 4.** The complex crystallizes from THF ( $-20^\circ\text{C}$ ) as yellow plates in the monoclinic space group  $P2_1/c$  with four ion pairs per unit cell. Crystallographic data are collected in Table I and a view of the anion is shown in Figure 2. The cation is shown in Figure 3. Key bond lengths and angles are given in Tables V and VI and positional parameters are given in Table VII. Although many crystals were examined, only a few were found to be of marginal quality for X-ray crystallography.

**Table VI.** Selected Bond Angles (deg) for **4**<sup>a</sup>

atom 1	atom 2	atom 3	angle	atom 1	atom 2	atom 3	angle
Fe	Rh	P1	50.6 (2)	Rh	P1	Fe	77.2 (3)
Fe	Rh	P2	110.5 (2)	Rh	P1	C8	117 (1)
Fe	Rh	C4	154 (1)	Rh	P1	C12	114.5 (8)
P1	Rh	P2	160.8 (3)	Fe	P1	C8	118 (1)
P1	Rh	C4	104 (1)	Fe	Pu	C12	119.0 (8)
P2	Rh	C4	95 (1)	C8	P1	C12	108 (1)
Rh	Fe	P1	52.2 (2)	Rh	P2	C5	120 (1)
Rh	Fe	C1	103 (1)	Rh	P2	C6	114 (1)
Rh	Fe	C2	144 (1)	Rh	P2	C7	117 (1)
Rh	Fe	C3	101 (1)	P3	O10	Na1	152 (2)
P1	Fe	C1	123 (1)	Fe	C1	O1	177 (3)
P1	Fe	C2	91 (1)	Fe	C2	O2	178 (3)
P1	Fe	C3	122 (1)	Fe	C3	O3	176 (3)
C1	Fe	C2	97 (2)	Rh	C4	O4	178 (3)
C1	Fe	C3	113 (2)	O10	P3	C26	114 (2)
C2	Fe	C3	98 (2)	O10	P3	C27	111 (2)
				O10	P3	C28	114 (2)

<sup>a</sup>Numbers in parentheses are estimated standard deviations in the least significant digits.

**Table VII.** Positional Parameters for **4**

	x	y	z	$B(\text{Å}^2)^a$
Rh	0.7000 (2)	0.2204 (2)	0.69342 (8)	3.27 (4)
Fe	0.8389 (3)	0.1917 (4)	0.6275 (1)	4.5 (1)
P1	0.6922 (6)	0.0792 (7)	0.6393 (3)	3.6 (2)
P2	0.7638 (7)	0.3745 (7)	0.7398 (3)	4.4 (2)
P3	1.1562 (8)	0.3221 (8)	0.5302 (3)	5.7 (2)
Na1	1.2418 (9)	0.561 (1)	0.6017 (4)	5.0 (3)
O1	1.047 (2)	0.148 (3)	0.6749 (8)	9.5 (7)*
O2	0.880 (2)	0.040 (2)	0.5532 (8)	8.2 (7)*
O3	0.813 (2)	0.435 (3)	0.585 (1)	11.3 (9)*
O4	0.505 (2)	0.159 (2)	0.7393 (7)	6.7 (6)*
O5	1.155 (2)	0.752 (2)	0.5756 (8)	8.9 (7)*
O6	1.378 (2)	0.698 (3)	0.5731 (8)	9.8 (7)*
O7	1.426 (2)	0.488 (2)	0.6251 (8)	8.1 (7)*
O8	1.238 (2)	0.433 (3)	0.665 (1)	11.6 (9)*
O9	1.111 (2)	0.637 (2)	0.6501 (7)	7.3 (6)*
O10	1.186 (2)	0.445 (2)	0.5491 (8)	8.2 (7)*
C1	0.962 (3)	0.168 (3)	0.654 (1)	8 (1)*
C2	0.861 (2)	0.105 (3)	0.584 (1)	5.6 (8)*
C3	0.828 (3)	0.332 (3)	0.604 (1)	6.9 (9)*
C4	0.584 (2)	0.183 (3)	0.722 (1)	5.4 (8)*
C5	0.701 (3)	0.399 (3)	0.789 (1)	6.6 (9)*
C6	0.909 (3)	0.356 (3)	0.760 (1)	5.7 (8)*
C7	0.762 (3)	0.540 (3)	0.718 (1)	5.8 (8)*
C8	0.570 (2)	0.088 (3)	0.5986 (9)	4.6 (7)*
C9	0.556 (3)	0.228 (3)	0.586 (1)	6.7 (8)*
C10	0.466 (3)	0.038 (4)	0.617 (1)	9 (1)*
C11	0.586 (3)	0.021 (4)	0.557 (1)	8 (1)*
C12	0.712 (2)	-0.096 (2)	0.6580 (8)	3.1 (6)*
C13	0.737 (2)	-0.182 (3)	0.621 (1)	5.3 (8)*
C14	0.618 (3)	-0.138 (3)	0.683 (1)	6.7 (9)*
C15	0.815 (2)	-0.091 (3)	0.6889 (9)	3.7 (6)*
C16	1.228 (3)	0.826 (4)	0.554 (1)	10 (1)*
C17	1.311 (3)	0.761 (4)	0.538 (1)	10 (1)*
C18	1.473 (4)	0.614 (4)	0.567 (1)	11 (1)*
C19	1.505 (3)	0.560 (4)	0.605 (1)	9 (1)*
C20	1.432 (3)	0.458 (4)	0.666 (1)	8 (1)*
C21	1.349 (4)	0.385 (5)	0.681 (2)	12 (1)*
C22	1.173 (3)	0.475 (4)	0.698 (1)	10 (1)*
C23	1.077 (3)	0.530 (4)	0.675 (1)	9 (1)*
C24	1.029 (3)	0.706 (4)	0.626 (1)	9 (1)*
C25	1.083 (3)	0.803 (4)	0.605 (1)	10 (1)*
C26	1.240 (4)	0.275 (5)	0.488 (1)	12 (1)*
C27	1.162 (3)	0.204 (4)	0.570 (1)	8 (1)*
C28	1.018 (4)	0.314 (4)	0.506 (1)	11 (1)*

<sup>a</sup>Atoms with an asterisk were refined isotropically. Anisotropically refined atoms are given in the form of the isotropic equivalent thermal parameter defined as  $(4/3)[a^2B(1,1) + b^2B(2,2) + c^2B(3,3) + ab(\cos \gamma)B(1,2) + ac(\cos \beta)B(1,3) + bc(\cos \alpha)B(2,3)]$ .

The crystals undergo considerable decay in the X-ray beam and so two were used for the data collection. A low-temperature ( $-100^\circ\text{C}$ ) data set gave no better results.

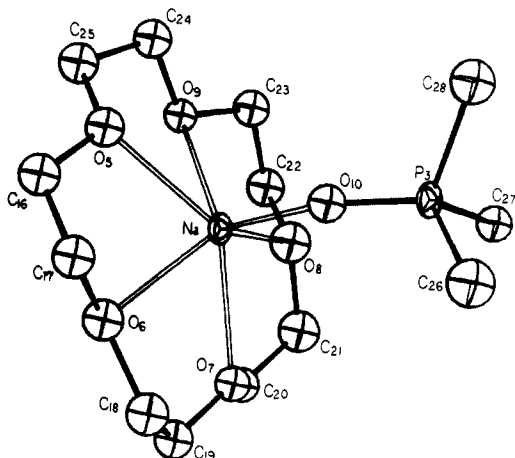


Figure 3. ORTEP view of the cationic moiety of **4** showing the atom numbering scheme. The atoms are shown at the 50% probability level.

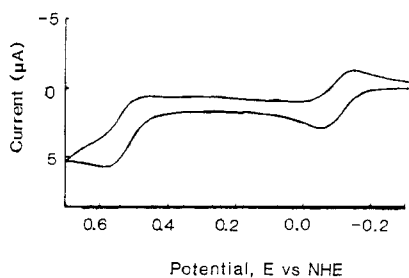


Figure 4. Oxidative voltammetry of 5.85 mM **2** in THF/0.4 M TBABF<sub>4</sub>. Scan rate = 200 mV/s.

The overall molecular structure of the anion is similar to those of the neutral Fe–Rh complexes. The central core consists of a *t*-Bu<sub>2</sub>P<sup>−</sup> group bridging an Fe–Rh bond (2.796 (5) Å) which is slightly longer than that found in **2** (2.665 (1) Å). However, it is still in the normal range for a single Fe–Rh bond.<sup>3c</sup> There are no bridging or semibringing CO units. The coordination geometry about the Rh atom is now a distorted square plane with the atoms Rh, Fe, P(1), P(2), and C(4) all virtually in the same plane.<sup>15</sup> The geometry about Fe can be described as a distorted trigonal bipyramid if the Fe–Rh bond is included. The atoms P(1), C(1), and C(3) occupy roughly equatorial positions while C(2) and the Rh atom lie on axial sites. There is a distortion from an idealized geometry since the Rh–Fe–C(2) angle is 144 (1)° instead of 180°. The metric parameters of the ion all fall within normal limits and require little further discussion.

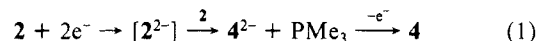
The cationic portion of **4** (Figure 3) consists of the Na<sup>+</sup> ion bound to all five oxygen atoms of the crown ether. The average Na–O distance is 2.43 Å. A sixth coordination site on the Na<sup>+</sup> ion is occupied by the oxygen of a Me<sub>3</sub>PO group. Here, the Na–O distance is notably shorter at 2.13 (3) Å. This is a reasonable distance considering the atomic radii of Na and O. The greater Na–O distances for the crown ether probably reflect the steric restraints encountered in coordinating all five oxygen atoms in one hemisphere of the Na<sup>+</sup> ion.

**Electrochemistry. Oxidations.** Solutions of **2** and **3** (THF/0.4 M TBABF<sub>4</sub>) both show two oxidation waves (Figure 4). In both cases, the first is reversible at  $\nu = 200$  mV/s, and  $E_{1/2}$  for the oxidation of **2** is  $-0.10$  V vs NHE; **3** is oxidized at 0.255 V. The second wave is irreversible (presumably due to a reaction following electron transfer) and is located at +0.650 V for both complexes. Similar oxidation potentials of other phosphido- and arsenido-bridged dimers have been observed,<sup>16</sup> and the behavior can be attributed to a localized oxidation of the electron-rich bridging atom.

**Reductions.** The reduction of **2** in THF/0.4 M TBABF<sub>4</sub> occurs

in a single irreversible wave at  $-2.28$  V (scan rate  $\nu = 1$  V/s, Figure 5a,c). On the anodic scan, three oxidations are seen, at  $-2.06$ ,  $-1.43$ , and  $-1.24$  V, and the current crosses over the cathodic scan if the switching potential is near the reduction peak. As shown in Figure 6a, the oxidation process at  $-2.06$  V is reversible, with near-Nernstian peak splitting ( $\Delta E_p = 80$  mV) being observed on a second scan. Ferrocene/ferrocenium under these circumstances in the same solution shows a similar  $\Delta E_p$ , so we attribute the peak splitting above the ca. 59 mV level to uncompensated resistance in this solvent. The oxidations at  $-1.43$  and  $-1.24$  V are irreversible and do not generate a new reducible species upon subsequent scans (Figure 5a).

A controlled potential electrolysis at  $-2.40$  V of 47.7 mg of **2** consumed 14.57 C ( $n_{app} = 1.95$ ), suggesting that an overall  $2e^-$  reduction of **2** occurs. Similarly, bulk electrolysis of **3** also consumes 2 f/mol. The NMR and ESR spectra of an aliquot of the electrochemically reduced solution are virtually identical with one prepared by sodium sand reduction of either **2** or **3** (see above), and on this basis, we assume that the stable reduction product generated electrochemically is **4**. The voltammetry of electrochemically generated **4** is shown in Figure 7. A reversible oxidation peak is seen at  $E_{1/2} = -1.20$  V with a larger oxidation wave at  $E_{1/2} = -0.94$  V. Significantly, no peaks at the same potentials as those seen in Figure 5 ( $-1.24$ ,  $-1.43$ , and  $-2.06$  V) are observed in Figure 7. Therefore, the species responsible for the oxidations shown in Figure 5 are only stable on the CV time scale, while **4** is the ultimate reduction product of **2** over a longer period of time. During the time scale of the electrolysis ( $\sim 1000$  s), an electron is released into solution and is consumed irreversibly (by reaction with impurities or THF), so that the overall stoichiometry of the bulk electrolysis is maintained ( $n_{app} = 2$ ). Since **2** has 3 CO ligands and **4** has 4, the mechanism of the formation of **4** during the reduction of **2** is complex; it requires the abstraction of CO from **2**, along with the loss of PMe<sub>3</sub> and an electron into solution, as shown in eq 1.



Repeated cycling between  $-1.85$  and  $-2.45$  V (Figure 6a) shows that the reduction peak at  $-2.28$  V corresponding to unreduced **2** disappears quickly and the voltammograms rapidly reach a steady-state response. However, at faster scans (10 V/sec.), the peak corresponding to the reduction of **2** is more persistent (Figure 6c), and the peak at  $-1.40$  V has virtually disappeared (Figure 5e). At 50 V/s (Figure 6e) an isopotential point<sup>4</sup> at  $-2.25$  V is observed, as expected for an ECE process in which homogeneous reactions associated with the redox chemistry are insignificant.

The electrochemical reduction of **3** in THF/0.4 M TBABF<sub>4</sub> is shown in Figure 8. A reduction wave is observed at  $-2.50$  V. As mentioned above, the reduction consumes 2 f/mol during bulk electrolysis at  $-2.7$  V. On the anodic scan, the reduction product shows a reversible ( $\Delta E_p = 70$  mV) oxidation wave at  $E_{1/2} = -1.80$  V. Two irreversible oxidations are also seen at  $-0.85$  and  $-1.05$  V. This is very similar to the behavior of **2**.

The structures of **2** and **3** have two different features: one phosphine molecule on the Rh atom is replaced with a CO, and **3** does not possess a CO bridging unit. Carbon monoxide substitution on the Rh atom should stabilize the reduced forms by increased  $\pi$ -back-bonding, thus shifting the reduction peak in the positive direction. On the other hand, the lack of a CO bridging unit would tend to destabilize the reduced form of **3** relative to **2**, and make **3** more difficult to reduce. The observed reduction potential of **3** suggests the latter effect is the more important.

The oxidation potential of the dianion is also influenced by the effects of  $\pi$ -back-bonding onto the terminal and bridging CO ligands on the Rh atom. We observe that the oxidation potential of the  $3^{2-}$  is shifted positive, which reflects the stabilizing effect of the terminal CO ligand on  $3^{2-}$ . Moreover, neither dianion appears to possess a  $\mu_2$ -CO bridge; otherwise,  $2^{2-}$  would be harder to oxidize than  $3^{2-}$ , as discussed above. Thus, the chemical reaction in the ECE reduction mechanism of **2** must involve some swinging motion of the CO bridging unit away from the Rh atom.

**Digital Simulations of the Voltammetry of 2.** The voltammo-

(16) (a) Dessy, R. E.; Kornmann, R.; Smith, C.; Haytor, R. J. *J. Am. Chem. Soc.* **1968**, *90*, 2001. (b) Whittlesley, B. R.; Chandler, D. J.; Moulton, R. D.; Jones, R. A.; Bard, A. J., unpublished results.

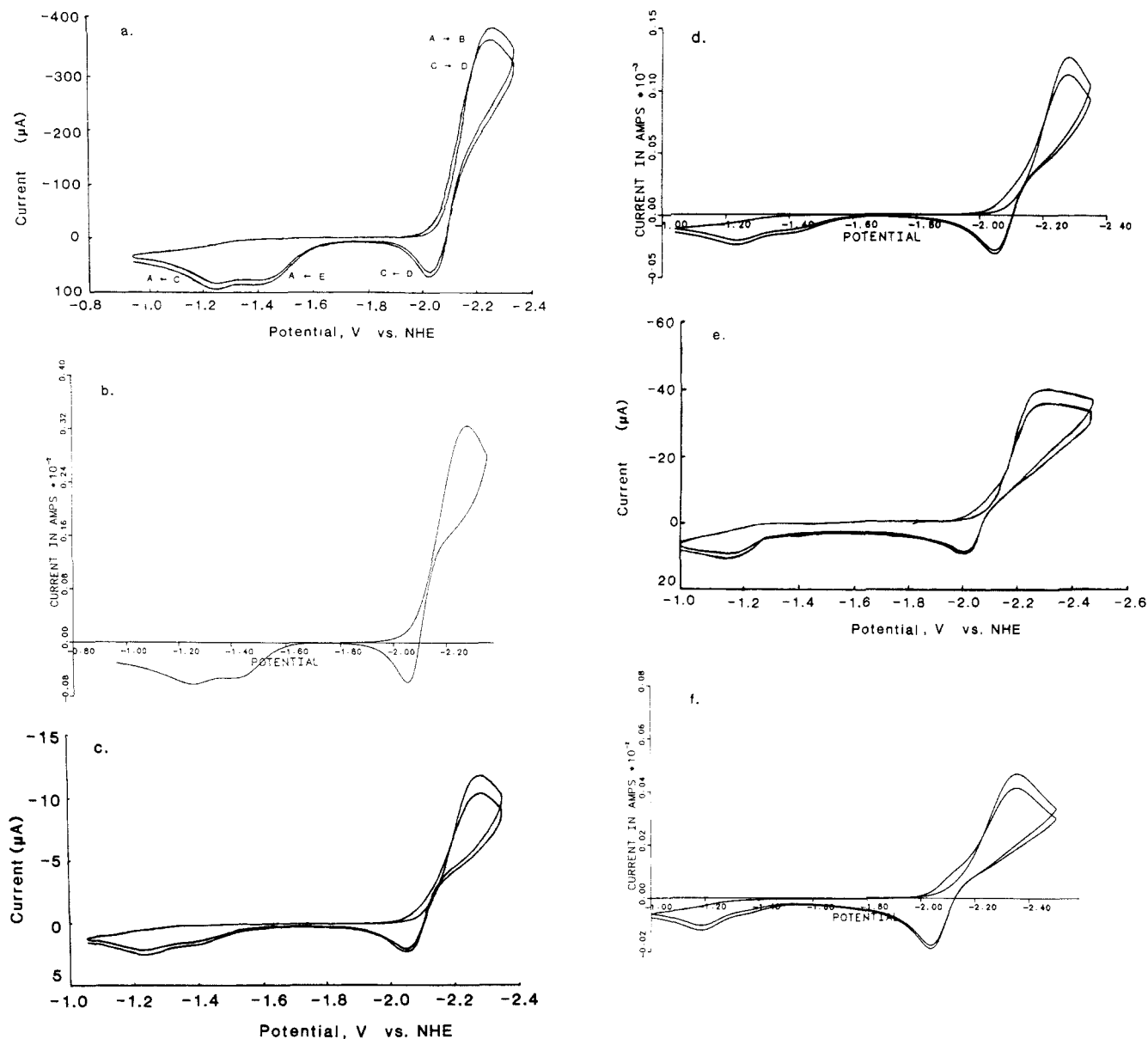
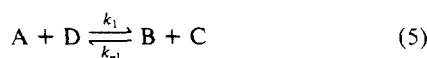
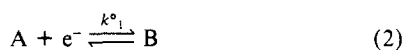


**Figure 5.** (a) Reduction of 18.1 mM **2** in THF/0.4 M TBABF<sub>4</sub>. Electrode area = 0.026 cm<sup>2</sup>. Scan rate = 1 V/s. (b) Digital simulation of the voltammogram in part a, based on the following input parameters:  $\alpha_1 = 0.40$ ;  $\alpha_2 = \alpha_3 = 0.50$ ;  $\alpha_4 = 0.40$ ;  $\Psi_1 = 6 \times 10^{-6}$ ;  $\Psi_2 = 2.5 \times 10^{-2}$ ;  $\Psi_3 = 7 \times 10^{-5}$ ;  $\Psi_4 = 2.3 \times 10^{-6}$ ;  $k_1 = 2.5 \times 10^3 \text{ M}^{-1} \text{ s}^{-1}$ ;  $k_2 = 7 \times 10^4 \text{ M}^{-1} \text{ s}^{-1}$ ;  $k_{-2} = 1.5 \times 10^5 \text{ M}^{-1} \text{ s}^{-1}$ ;  $k = 800 \text{ s}^{-1}$ ;  $E_{1/2}^1 = -1.815 \text{ V}$ ;  $E_{1/2}^2 = -2.075 \text{ V}$ ;  $E_{1/2}^3 = -1.670 \text{ V}$ ;  $E_{1/2}^4 = -1.820 \text{ V}$ ; concentration = 18.1 mM;  $\nu = 1 \text{ V/s}$ ; electrode area = 0.026 cm<sup>2</sup>;  $D_0 = 4.8 \times 10^{-6} \text{ cm}^2 \text{ s}^{-1}$ . (c) Reduction of 5.85 mM **2** in THF/0.4 M TBABF<sub>4</sub>. Scan rate = 1 V/s; electrode area = 0.00204 cm<sup>2</sup>. (d) Digital simulation of the voltammogram in part c, with the same input variables as in part b, except that  $\alpha_1 = 0.55$ ;  $\alpha_3 = 0.40$ ;  $\Psi_1 = 7 \times 10^{-7}$ ;  $\Psi_2 = 4 \times 10^{-2}$ ;  $\Psi_3 = 10^{-5}$ ;  $\Psi_4 = 8 \times 10^{-6}$ ; concentration = 5.85 mM; electrode area = 0.00204 cm<sup>2</sup>. (e) Voltammogram as in part c, but with scan rate = 10 V/s. (f) Digital simulation of the voltammogram in part e, with input variables as in part d, except  $\alpha_1 = 0.39$ ;  $\Psi_1 = 2 \times 10^{-5}$ ;  $\Psi_2 = 7 \times 10^{-3}$ ;  $\Psi_3 = 10^{-6}$ ;  $\Psi_4 = 8 \times 10^{-7}$ ;  $\nu = 10 \text{ V/s}$ ;  $k = 2000 \text{ s}^{-1}$ .

grams are qualitatively similar to those seen with [Rh( $\mu_2$ -*t*-Bu<sub>2</sub>P)(CO)<sub>2</sub>]<sub>2</sub> and this suggests that the reduction mechanism might be elucidated by digital simulation. Previous results<sup>4</sup> suggest an ECE-DISP1 mechanism as a starting point for modeling the voltammetry (eq 2–5). The crossover observed in the reduction of **2** in Figure 5c is also consistent with this mechanism.<sup>8c,10a</sup> In the equations below A represents starting material (**2** or **3**) and B, C, D, ..., represent intermediates formed during the reduction. The reactions are identified with the different waves in Figure 5a.



On the anodic scan, we see the oxidation of D back to C. C can be oxidized at a more positive potential, followed by the reverse isomerization.<sup>4</sup>



Since the conversion of F to A is much faster than the equivalent time window of the CV scan, we treat the oxidation of C to A in the simulation as a single process:



The additional peak that appears at lower scan rates at -1.43 V suggests an additional species (E) is formed in solution. The magnitude of the peak increases under similar scan rates with increasing concentration relative to the oxidation at -1.24 V (compare parts a and c of Figure 5), suggesting E is produced



via a second-order homogeneous reaction. The simulation program was amended to allow for new reactions, and the best fit to the experimental data was achieved by inclusion of eq 9 and 10.



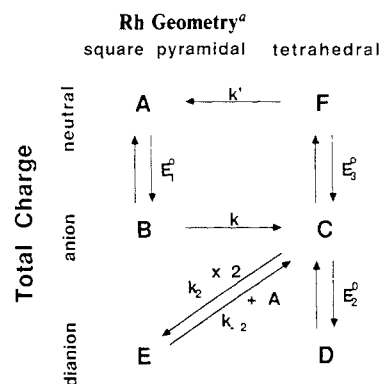
A successful digital simulation requires good agreement with experimental data over a wide range of experimental conditions: scan rate, multiple scans, concentration, and switching potential. From the voltammograms it is apparent that, with the exception of the reversible wave observed at  $-2.10$  V, all of the heterogeneous electron-transfer processes are totally irreversible. The transfer coefficients for the irreversible waves were chosen to match the observed voltammograms.<sup>17</sup> The heterogeneous electron-transfer rates  $k^{\circ}$  and the redox potentials  $E^{\circ}$  for the irreversible processes were chosen to give the peak potential vs scan rate behavior observed in Figure 5 (a large number of pairs of  $E^{\circ}$  and  $k^{\circ}$  values is consistent with this observed behavior, thus our values are arbitrary). The heterogeneous rate constant of the reversible process at  $-2.10$  V was set at the value that produces a quasireversible wave with the observed peak splitting ( $\Delta E_p$ ). As mentioned earlier, the source of the peak splitting is probably uncompensated resistance in solution rather than sluggish heterogeneous electron-transfer kinetics. However, these two effects give virtually identical voltammetric behavior.<sup>18</sup>

The agreement between the simulated and observed voltammograms was closest when we assigned the following values to the rate constants:  $k_1 = 2.5 \times 10^3 \text{ M}^{-1} \text{ s}^{-1}$ ,  $k_2 = 7 \times 10^4 \text{ M}^{-1} \text{ s}^{-1}$ , and  $k_{-2} = 1.5 \times 10^5 \text{ M}^{-1} \text{ s}^{-1}$ . Any values of  $k$  and  $k_{-1}$  that satisfy the relations  $k \gg k_{-1}C^{\circ}$  and  $k > 600 \text{ s}^{-1}$  will give a satisfactory fit. Simulated voltammograms (Figures 5b,d,f and 6b,d,f) can be compared to the respective observed voltammograms (Figures 5a,c,e and 6a,c,e). Of particular importance is the rapid approach to steady-state response observed on multiple reversals. This is an expression of the fast rate of eq 5. Note also the crossover observed in Figure 5c, which is characteristic of an ECE-DISP1 mechanism.<sup>8c,10</sup> The appearance of E agrees with observed behavior with respect to changes in scan rate and concentration. There is a small background contribution to the current, which is responsible for distorting the shape of the reduction waves, especially at higher scan rates (since the peak shifts to more negative potentials into this background). This background is more clearly resolved and can be seen separately at lower scan rates, as in Figure 6a.

The simulations show that the oxidation peak for E ( $-1.42$  V) has many of the characteristics of a CE process:<sup>19</sup> the equilibrium in eq 10 lies to the left, so that E and A are thermodynamically unstable with respect to 2C. However, E is easier to oxidize than C, so E is formed dynamically (in a reaction layer near the electrode surface) as the electrode potential is swept past this wave. The possible conversion of D to E during the CV time scale was examined as a possible contribution to the electrochemical mechanism, but the digital simulations of this possible reaction in the electrochemical mechanism give an unsatisfactory result when compared with the effect of substrate concentration, as seen in Figure 5, a and c. The non-interconversion of D and E suggests that they possess significantly different molecular geometries.

**Proposed Structures of A-F.** The similarity between the electrochemical behavior for the reduction of **2** and  $[Rh(\mu_2-t-Bu_2P)(CO)_2]_2$  suggests that similar geometrical isomerizations are responsible for the chemical steps of the ECE mechanism. For a clearer illustration of the nature of the proposed intermediates, we present Schemes III and IV, in which conversions between redox states (neutral, anion radical, and dianion) and geometric isomers (square-pyramidal and tetrahedral Rh) are shown. As

Scheme IV



<sup>a</sup>The proposed structure of E is distorted tetrahedral with a zero Rh-Fe bond order (see text).

noted above, there is an additional complication when one considers the coordination geometry about Rh. If one includes both the Fe-Rh bond and the bridging CO ligand in the coordination sphere, then it has a distorted square-based pyramidal geometry. However, if the bridging CO swings back to bind to only the Fe atom, then the coordination geometry at Rh is distorted square planar. We propose that this motion is accompanied by a movement of both Rh- $PMe_3$  ligands to give the Rh atom a distorted tetrahedral geometry in the conversion of B to C. Conversion to the dianion D then occurs with the geometry at Rh remaining roughly tetrahedral. Upon oxidation, the neutral form of the tetrahedral species F is formed from C, but this rapidly converts to the original form A, since no reduction peak is seen on the next scan. The isomerization of F to A is essentially achieved by a reversal of that which occurs for B to C. A CO ligand now swings into the coordination sphere of the Rh atom and in order to accommodate it, the Rh- $PMe_3$  groups are forced to line up more or less in the Rh-Fe-P(1) plane as found in the X-ray structure of **2**. The lack of a CO bridging unit in the D form is also consistent with the differences in the oxidation potentials of the D forms of **2** and **3**, as mentioned above.

We have now mentioned all possible oxidation states and geometries for the Fe-Rh complexes, except the dianion E. From the electrochemical studies, and we know that E is a dianion but it will not interconvert readily with D. This suggests that it has a significantly different molecular geometry than that of D. We also know that E is readily oxidized by a two-electron process to A. We propose that the structure of E does contain a tetrahedral Rh atom, consistent with it being a dianion and also by analogy to the behavior of  $[Rh(\mu_2-t-Bu_2P)(CO)_2]_2$ . However, as shown in Scheme III, we propose that the coordination environment about Rh now includes the carbon atom of a bridging CO ligand. In order for this to bind to the Rh atom, both Rh- $PMe_3$  groups must return to their sites as found in A or **2**. Thus it belongs to the same family of complexes as A and B, and we illustrate this in Schemes III and IV. We have depicted E with no Fe-Rh bond since none is required for each metal to achieve an 18 electron configuration. However, this "non-bond" may actually consist of fully occupied bonding and antibonding molecular orbitals. The latter is the HOMO of the molecule, and this may explain the ready oxidation of E to A, since the energy gained by the formation of a metal-metal bond provides the driving force for the simultaneous transfer of two electrons. On the other hand, when several electroactive centers are noninteracting, or when there is an electrostatic interaction, a sequential transfer of electrons is expected.<sup>20</sup> The geometries of E and D as depicted are sufficiently different that one would expect them to be relatively stable with respect to interconversion.

As we have previously discussed, the reduction of **2** and **3** produces **4** in good yield. Since the bulk electrolysis experiment

(17) Nicholson, R. S.; Shain, I. *Anal. Chem.* **1964**, *36*, 706.

(18) Nicholson, R. S. *Anal. Chem.* **1965**, *37*, 667.

(19) (a) Saveant, J. M.; Vianello, E. *Electrochem. Acta* **1963**, *8*, 905. (b) Saveant, J. M.; Vianello, E. *Electrochem. Acta* **1967**, *12*, 629.

(20) Itaya, K.; Bard, A. J.; Szwarc, M. *Z. Phys. Chem. Neue Folge* **1978**, *112*, 1.

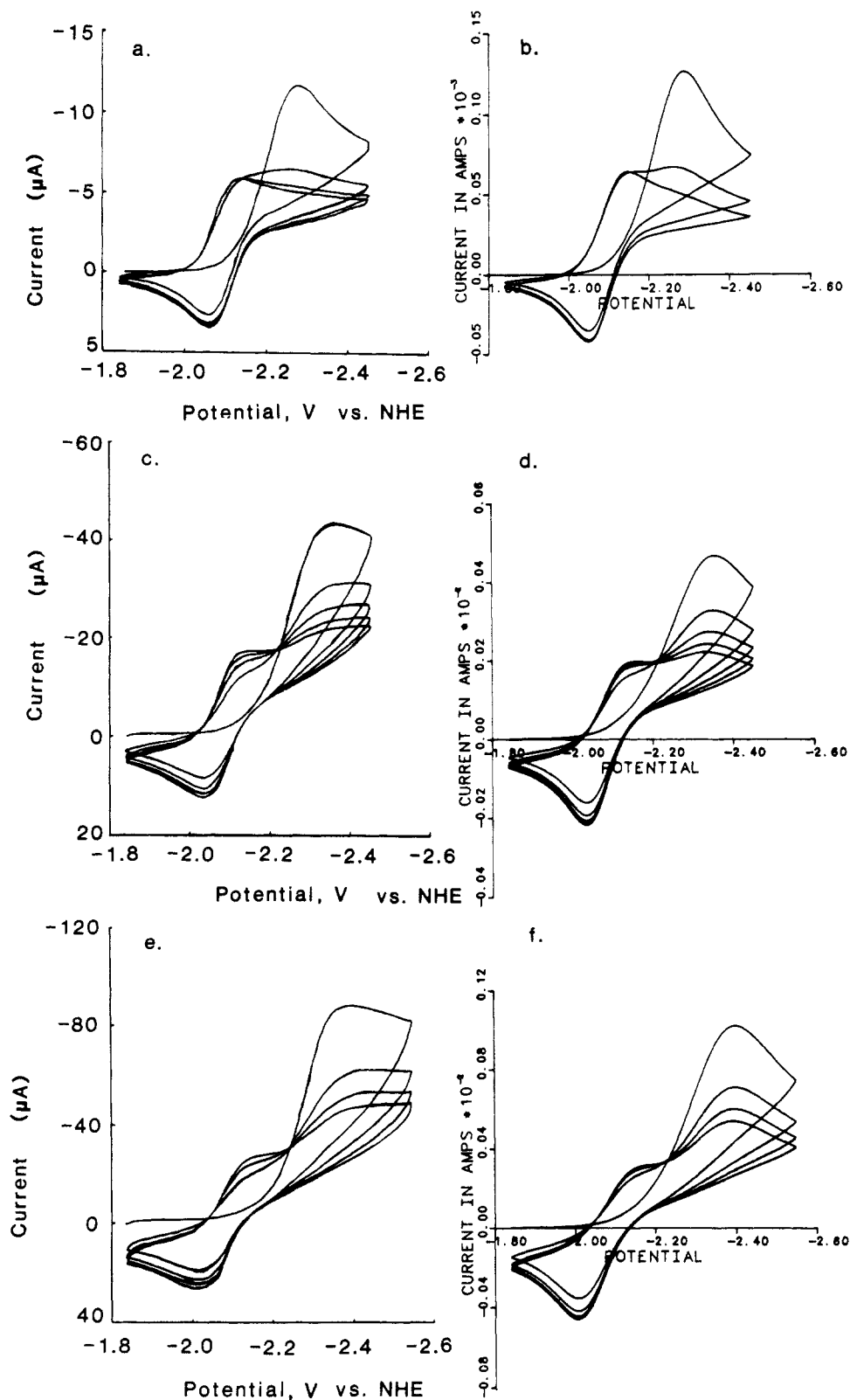


**Figure 6.** (a) Reduction and reoxidation of 5.85 mM **2** in THF/0.4 M TBABF<sub>4</sub>. Scan rate = 1 V/s. (b) Digital simulation of the voltammogram in part a, with input variables as in Figure 5d. (c) Same as Figure 6a, but with scan rate = 10 V/s. (d) Digital simulation of part c, with input variables as in Figure 5f. (e) Same as part a, but with scan rate = 50 V/s. (f) Digital simulation of the voltammogram in part e, with input variables as in Figure 5d, except  $\alpha_1 = 0.37$ ;  $\Psi_1 = 7 \times 10^{-2}$ ;  $\Psi_2 = 1.1 \times 10^{-3}$ ;  $\nu = 50 \text{ V s}^{-1}$ ;  $k = 10000 \text{ s}^{-1}$ .

consumes 2.0 f/mol we conclude that a dianion species reacts to generate **4** in THF (eq 1). In the discussion above we propose that the reduction of **2** or **3** produces (on the CV time scale) a dianion analogue of **4**. Our electrochemical studies have shown that **4** is not reducible within the potential window of THF, so we conclude the dianion analogue of **4** is oxidized spontaneously by the solvent to form **4** as an anion radical. Loss of PMe<sub>3</sub> from

**2** or **3** during both bulk electrolysis and the sodium reduction is consistent with the increased charge on the metal and the phosphine acting as a good  $\sigma$  donor but a poor  $\pi$  back acceptor relative to CO.

In the case of **3**, a simple loss of PMe<sub>3</sub> during reduction can result in the formation of **4**. On the other hand, the formation of **4** via reduction of **2** is more complex, since an abstraction of

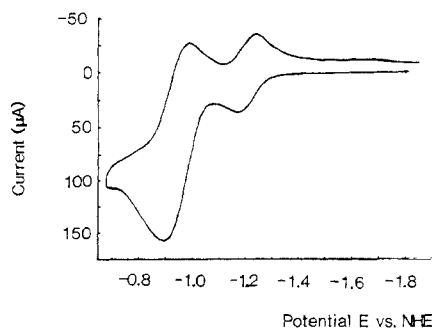


Figure 7. Electrochemical oxidation of 16 mM **4** in THF/0.2 M TBA-PF<sub>6</sub>. Scan rate = 1 V/s. Electrode area = 0.026 cm<sup>2</sup>.

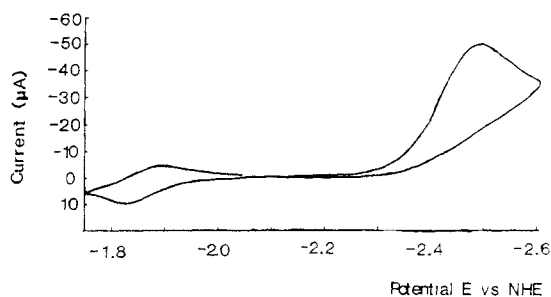


Figure 8. Electrochemical reduction of 3.96 mM **3** in THF/0.4 M TBABF<sub>4</sub>. Scan rate = 500 mV/s. Electrode area = 0.026 cm<sup>2</sup>.

a CO ligand in solution is required (**4** has 4 CO molecules; **2** has only 3). The result can be rationalized with our observation<sup>21</sup> that the Rh(CO)(PR<sub>3</sub>) moiety is relatively stable and unreactive with respect to further reaction with CO and phosphines. Thus, for example, **1** reacts with excess PMe<sub>3</sub> to form **3** and not **2**, while **2** reacts with CO to form **3** and not **1**. Therefore, it appears that the thermodynamics favor the formation of **4**, which contains the Rh(CO)(PMe<sub>3</sub>) unit, via a decarbonylation reaction with unreduced **2**. Rh phosphine complexes are known to abstract CO from organometallic complexes.<sup>22</sup> The precise mechanism by which **4** is formed during the reduction of **2** is no doubt complex.

**Conclusions.** In this paper, we present the electrochemistry of some Fe-Rh dimers and demonstrate that the results can be accounted for by an ECE-DISP1 mechanism coupled to a second-order homogeneous reaction. The evidence for this assignment centers on the close agreement of the digital simulations of the cyclic voltammetry based on the proposed mechanism and the experimental CVs. The key to the use of this approach to solve problems in electrochemistry is to choose a wide range of experimental conditions for the CVs. In our example, information about the mechanism was obtained by studying the effects of changes in scan rate, switching potential, concentration, and multiple cycles. In general, these changes provide the necessary data to distinguish between similar possible mechanisms.

Overall, the electrochemical mechanism is similar to that previously observed with [Rh(μ<sub>2</sub>-*t*-Bu<sub>2</sub>P)(CO)<sub>2</sub>]<sub>2</sub>. In the present case, the simulations show that initially ECE-DISP1 reduction of **2** is associated with a second order reaction involving the formation of another dianionic species, E. However, in the present system there is an additional complication due to the different possible coordination geometries about Rh. The point implied by the electrochemical mechanism which needs to be addressed is if C possesses a different Rh geometry than either A or E (as implied by the electrochemical mechanism) why should the rate of eq 10 be so fast? The relatively high rates for both of the second-order reactions is in contrast to [Rh(μ<sub>2</sub>-*t*-Bu<sub>2</sub>P)(CO)<sub>2</sub>]<sub>2</sub> and to our studies<sup>23</sup> of the isoelectronic species (*t*-Bu<sub>2</sub>PH)-

(CO)<sub>2</sub>Fe(μ<sub>2</sub>-*t*-Bu<sub>2</sub>P)(μ<sub>2</sub>-CO)Rh(COD) (COD = 1,5-cyclo-octadiene). The electrochemical behavior of these molecules suggests that the comproportionation reaction (eq 8) is far slower and is only a minor perturbation of the basically ECE reduction process, whereas the formation of species E (eq 10) does not occur at all.

The relatively large values of the second-order rate constants of eq 5 and 10 in the case of **2** may be attributed in part to a greater stability of the intermediate species B and C. The equilibrium of eq 5 lies to the left (A + D) side for all ECE mechanisms, on the assumption the standard reduction potential of A is more negative than the reduction potential of C. The instability of B with respect to C (eq 3) shifts the equilibrium toward the forward reaction. For complex **2**, we may speculate that B (a square-based pyramidal Rh anion radical) is not as unfavorable a structure for the intermediate as it is in [Rh(μ<sub>2</sub>-*t*-Bu<sub>2</sub>P)(CO)<sub>2</sub>]<sub>2</sub> or in (*t*-Bu<sub>2</sub>PH)(CO)<sub>2</sub>Fe(μ<sub>2</sub>-*t*-Bu<sub>2</sub>P)(μ<sub>2</sub>-CO)-Rh(COD). Thus, one may consider **2** and **3** to have relatively flexible geometries and one can explain the transient formation of E via the reaction in eq 10 as an expression of flexibility in species C.

The structural differences of **2** and **3** compared to [Rh(μ<sub>2</sub>-*t*-Bu<sub>2</sub>P)(CO)<sub>2</sub>]<sub>2</sub> do not greatly alter the reaction scheme from ECE-DISP1. This suggests the role of the second metal is as an "innocent" ligand, and that the square-based pyramidal Rh atom alone is responsible for the interesting electrochemical mechanism. The Fe atom does participate in the slower reaction that forms **4**. By contrast, the bulk electrolysis of [Rh(μ<sub>2</sub>-*t*-Bu<sub>2</sub>P)(CO)<sub>2</sub>]<sub>2</sub> produces a stable dianion. Other Rh heterobimetallics might show similar behavior. By comparing the electrochemical behavior of these molecules with other analogous complexes, more connections between structure and reactivity may become clear.

#### Experimental Section

**Chemicals.** Tetra-*n*-butylammonium fluoroborate (TBABF<sub>4</sub>) (Southwestern Chemicals) was recrystallized once from methanol slowly (to remove impurities) and once from THF/ether quickly (to remove trapped solvent) and was dried under vacuum and stored in a desiccator. Hexane, tetrahydrofuran (THF), and diethyl ether were dried over sodium and distilled from sodium benzophenone ketyl under nitrogen before use. Toluene was freshly distilled from sodium metal under nitrogen. RhCl(PMe<sub>3</sub>)<sub>3</sub>,<sup>24</sup> (Rh(CO)<sub>2</sub>Cl)<sub>2</sub>,<sup>25</sup> and *t*-Bu<sub>2</sub>PH<sub>2</sub><sup>26</sup> were prepared by literature procedures. Melting points were in sealed capillaries under nitrogen (1 atm) and are uncorrected. All reactions were performed under oxygen-free nitrogen or under vacuum. Microanalyses were by the Schwartzkopf Microanalytical Laboratory, Woodside, NY.

**Measurements.** IR: Perkin-Elmer 1330. NMR: Varian EM-390 (<sup>1</sup>H, 90 MHz), FT-80 (<sup>31</sup>P, 32.384 MHz), Bruker WM-90 (<sup>31</sup>P, 36.43 MHz), Nicolet NT-200 (<sup>1</sup>H and <sup>31</sup>P). ESR: Varian E-9 spectrometer (100 kHz field modulation), equipped with a TE<sub>102</sub> dual-sample cavity. IR spectra were taken as Nujol mulls (KBr plates) or in solution (matched KBr or CaF<sub>2</sub> cells). NMR spectra were recorded in C<sub>6</sub>D<sub>6</sub> at ambient temperature unless otherwise stated and are referenced to Me<sub>4</sub>Si (δ 0.0, <sup>1</sup>H) and 85% H<sub>3</sub>PO<sub>4</sub>(aq) (δ 0.0, <sup>31</sup>P, downfield is positive).

Electrochemical measurements were made with equipment previously described.<sup>4</sup> Scan rates faster than 1 V/s were recorded with a Nicolet digital oscilloscope. The working electrode used for the measurements was a J-shaped Pt wire<sup>27</sup> imbedded in glass (working area = 0.204 mm<sup>2</sup>); a Pt flag counter electrode and an Ag wire reference were used, except where noted otherwise. Bulk electrolysis was performed at a Pt mesh (area = 5 cm<sup>2</sup>). The cell was of a three-compartment design as described previously.<sup>28</sup>

Blank solutions of THF and supporting electrolyte were prepared under N<sub>2</sub> and transferred to the cell via cannulae. If the background of the solution was acceptable, an aliquot was removed from the working compartment and added to a weighed quantity of the Fe-Rh dimer. As soon as the compound had dissolved, the mixture was returned to the cell and electrochemical experiments were performed. After the experiments were done, a small quantity of ferrocene was added as an internal standard for measurement of the reference potential. All potentials are

(21) Other μ<sub>2</sub>-phosphido-bridged Rh complexes exhibit this effect. Arif, A. M.; Heaton, D. H.; Jones, R. A.; Nunn, C. A., manuscript in preparation.

(22) Cotton, F. A.; Wilkinson, G. *Advanced Inorganic Chemistry*; Wiley: New York, 1980; pp 936-940, 1297-1298, and references therein.

(23) Moulton, R. D.; Chandler, D. J.; Jones, R. A.; Bard, A. J., unpublished results.

(24) Jones, R. A.; Mayor-Real, F.; Wilkinson, G.; Galas, A. M. R.; Hursthouse, M. B.; Malik, K. M. A. *J. Chem. Soc., Dalton Trans.* **1980**, 511.

(25) McCleverty, J. A.; Wilkinson, G. *Inorg. Synth.* **1966**, 8, 211.

(26) Hoffman, H.; Schellenbeck, P. *Chem. Ber.* **1966**, 99, 11.

(27) Bard, A. J. *Anal. Chem.* **1961**, 33, 11.

(28) Van Duyne, R. P.; Reilly, C. N. *Anal. Chem.* **1972**, 44, 142.

referenced to ferrocene/ferrocenium (taken as +0.547 V vs NHE).<sup>29</sup>

**Digital Simulations.** The simulated voltammograms were generated by using the program and method described previously.<sup>4</sup> The program was run on the CDC Dual Cyber 170/750 system at the University of Texas. The program was amended to incorporate the new reactions associated with the presence of E. The generation of A and E in homogeneous solution was modeled by bimolecular decay of two molecules of C separately from the flux calculations.

The faradaic flux for the new mechanism (eq 2-10) is as follows:

$$f_{\text{far}} = k_{\text{F1}}C_{\text{A}}(x=0) - k_{\text{B1}}C_{\text{B}}(x=0) - k_{\text{B3}}C_{\text{C}}(x=0) - k_{\text{B4}}C_{\text{E}}(x=0) + k_{\text{F2}}C_{\text{C}}(x=0) - k_{\text{B2}}C_{\text{D}}(x=0) \quad (11)$$

In converting to the notation of the finite difference method of digital simulations, the expression

$$C_j(x=0) = C_j(1) - \frac{\Delta x(f_j)_{x=0}}{2D_j} \quad (12)$$

is used to define the faradaic flux in terms of the fluxes of the individual species, along with the heterogeneous and simulation parameters. Solving for  $(f_{\text{B}})_{x=0}$  and  $(f_{\text{E}})_{x=0}$  gives the following expressions:

$$(f_{\text{B}})_{x=0} = \frac{\chi_0 - \epsilon_0 - \zeta_0\epsilon_1 - \beta_0\epsilon_1 + \epsilon_1\zeta_1(f_{\text{C}})_{x=0} + \epsilon_1\beta_1(f_{\text{E}})_{x=0}}{1 + \chi_1 + \epsilon_1} \quad (13)$$

$$(f_{\text{E}})_{x=0} = \frac{\beta_0}{1 + \beta_1} \quad (14)$$

where  $\beta_0 = k_{\text{B4}}C_{\text{E}}(1)$ ,  $\beta_1 = k_{\text{B4}}\Delta x/2D_{\text{E}}$ , and  $k_{\text{B4}}$  is the heterogeneous rate constant for the oxidation of E to A (we are assuming the oxidation is totally irreversible). The expressions for  $(f_{\text{A}})_{x=0}$ ,  $(f_{\text{C}})_{x=0}$ , and  $(f_{\text{D}})_{x=0}$  and the other parameters are unchanged and are given in ref 4. The faradaic flux is then calculated from

$$f_{\text{far}} = (f_{\text{A}})_{x=0} - (f_{\text{D}})_{x=0} \quad (15)$$

where  $(f_{\text{A}})_{x=0}$  is dependent on the new expression for  $(f_{\text{B}})_{x=0}$  (eq 13).

**Synthesis of  $(\text{CO})_3(t\text{-Bu}_2\text{PH})\text{Fe}(\mu_2\text{-}t\text{-Bu}_2\text{P})\text{Rh}(\text{CO})_2$  (1).** A solution of *n*-BuLi was added to a solution of  $\text{Fe}(\text{CO})_3(t\text{-Bu}_2\text{PH})_2$  (2.32 mmol) in THF (40 mL) at  $-78^\circ\text{C}$  and allowed to warm to  $10^\circ\text{C}$  over 10 min. The solution was then recooled to  $-78^\circ\text{C}$  and added dropwise to a solution of  $(\text{Rh}(\text{CO})_2\text{Cl})_2$  (0.45 g, 1.16 mmol) in THF (40 mL). The dark red solution was allowed to warm to room temperature (2 h) during which time the color changed to yellow brown. Volatile materials were removed under vacuum and the residue extracted into hexane ( $3 \times 30$  mL). The solution was filtered and reduced in volume under vacuum (40 mL). Cooling ( $-20^\circ\text{C}$ , 24 h) gave green microcrystalline **1**. The crystals were collected and dried under vacuum. Yield 0.77 g, 43%; mp  $240\text{--}242^\circ\text{C}$ . IR (hexane solution, KBr plates): 2321 (m), 2040 (s), 2021 (s), 1980 (vs), 1923 (s), 1864 (s)  $\text{cm}^{-1}$ .  $^1\text{H}$  NMR ( $\text{C}_6\text{D}_6$ ,  $25^\circ\text{C}$ ):  $\delta$  4.14 (d,  $J_{\text{P-H}} = 335.7$  Hz, 1 H, *t*-Bu<sub>2</sub>PH), 1.52 (d,  $^3J_{\text{P-H}} = 13.5$  Hz, 18 H, *t*-Bu<sub>2</sub>P), 1.31 (d,  $^3J_{\text{P-H}} = 13.5$  Hz, 18 H, *t*-Bu<sub>2</sub>P).  $^{31}\text{P}$  NMR (THF,  $25^\circ\text{C}$ ):  $\delta$  239.82 (dd,  $J_{\text{P-Rh}} = 103.34$  Hz,  $^2J_{\text{P-P}} = 24.64$  Hz, *PBu*<sub>2</sub>), 96.74 (d,  $^2J_{\text{P-P}} = 24.38$  Hz, *Fe-PMe*<sub>3</sub>). In the proton coupled spectrum, a broad doublet is observed ( $J_{\text{P-H}} = 339.58$  Hz). Microanalysis: Calcd for  $\text{C}_{22}\text{H}_{37}\text{FeRhO}_3\text{P}_2$ : C, 42.90; H, 6.30. Found: C, 42.74; H, 6.14.

**Synthesis of  $(\text{CO})_2(\text{PMe}_3)\text{Fe}(\mu_2\text{-}t\text{-Bu}_2\text{P})(\mu_2\text{-CO})\text{Rh}(\text{PMe}_3)_2$  (2).** A solution of  $(\text{CO})_3\text{Fe}(t\text{-Bu}_2\text{PH})(t\text{-Bu}_2\text{PLi})$  (0.57 mmol) was prepared as described above and added dropwise at  $-78^\circ\text{C}$  to a solution of  $\text{RhCl}(\text{PMe}_3)_3$  (0.21 g, 0.57 mmol) in THF (40 mL). The dark green solution was allowed to warm to room temperature over 2 h and the color gradually changed to yellow-brown. Volatile materials were removed under vacuum and the residue extracted with hexane ( $2 \times 25$  mL). The solution was filtered and the volume reduced to ca. 20 mL under vacuum. Cooling ( $-20^\circ\text{C}$ ) gave orange crystals after 24 h. Yield 0.15 g (44%); mp  $115\text{--}117^\circ\text{C}$  dec. IR (hexane solution, KBr plates): 1950 (s), 1902 (s), 1735 (mbr)  $\text{cm}^{-1}$ .  $^1\text{H}$  NMR:  $\delta$  1.56 (d,  $^2J_{\text{P-H}} = 13.5$  Hz, 9 H, *Fe-PMe*<sub>3</sub>), 1.20, s, 18 H, *Bu*<sub>2</sub>P), 0.95, (dd,  $^2J_{\text{P-H}} = 12.0$  Hz, 18 H, *Rh-PMe*<sub>3</sub>).  $^{31}\text{P}$  NMR (THF, 121.482 MHz):  $\delta$  195.86 (ddt,  $J_{\text{P-Rh}} = 235.59$  Hz,  $^2J_{\text{P-P}} = 115.34$  Hz,  $^2J_{\text{P-P}} = 21.86$  Hz, *PBu*<sub>2</sub>), 31.51 (d,  $^2J_{\text{P-P}} = 21.86$  Hz, *Fe-PMe*<sub>3</sub>),  $-15.98$  (ddd,  $J_{\text{P-Rh}} = 234.98$  Hz,  $^2J_{\text{P-P}} = 115.34$  Hz,  $^2J_{\text{P-P}} = 40.07$  Hz, *trans-Rh-PMe*<sub>3</sub>),  $\delta$   $-20.07$  (ddd,  $J_{\text{P-Rh}} = 200.61$  Hz,  $^2J_{\text{P-P}} = 40.07$  Hz,  $^2J_{\text{P-P}} = 21.86$  Hz, *cis-Rh-PMe*<sub>3</sub>). Microanalysis: Calcd for  $\text{C}_{20}\text{H}_{45}\text{FeO}_3\text{P}_4\text{Rh}$ : C, 38.98; H, 7.36; P, 20.11. Found: C, 38.77; H, 7.40; P, 19.95.

**Synthesis of 2 from  $(\text{CO})_2(\text{Bu}_2\text{PH})\text{Fe}(\mu_2\text{-}t\text{-Bu}_2\text{P})(\mu_2\text{-CO})\text{Rh}(\text{COD})$  ( $\text{COD} = 1,5\text{-Cyclooctadiene}$ ).** To a THF (40 mL) solution of  $(\text{CO})_3\text{-}(\text{Bu}_2\text{PH})\text{Fe}(\mu_2\text{-}t\text{-Bu}_2\text{P})\text{Rh}(\text{COD})$  (0.53 g, 0.72 mmol) was added a large

excess of *PMe*<sub>3</sub> (4 mL, 40 mmol) and the solution was allowed to stir. A gradual color change from yellow-brown to dark-red was observed. After 3 h, the volatile materials were removed under vacuum and the residue recrystallized from hexane. Yield = 0.40 g (91%).

**Synthesis of  $(\text{CO})_3(\text{PMe}_3)\text{Fe}(\mu_2\text{-}t\text{-Bu}_2\text{P})\text{Rh}(\text{CO})(\text{PMe}_3)$  (3).** From **1**: *PMe*<sub>3</sub> (2 mL, 20 mmol) was added to a solution of **1** (0.40 g, 0.52 mmol) in THF (40 mL) at room temperature. The color immediately changed from green to red. The solution was stirred (3 h) at room temperature. Volatile materials were then removed under vacuum and the residue extracted into hexane ( $3 \times 30$  mL). The resulting solution was filtered and concentrated under vacuum (20 mL). Cooling ( $-20^\circ\text{C}$ , 12 h) gave large yellow prisms of **3** which were collected and dried under vacuum. Yield 0.30 g, 92%; mp  $140\text{--}142^\circ\text{C}$  dec. IR (hexane solution, KBr plates): 1960 (s), 1938 (s), 1870 (s), 1850 (s)  $\text{cm}^{-1}$ .  $^1\text{H}$  NMR (in  $\text{C}_6\text{D}_6$  at  $25^\circ\text{C}$ ):  $\delta$  1.51 (d,  $J_{\text{P-H}} = 13.0$  Hz, 18 H, *t*-Bu<sub>2</sub>P), 1.22 (d,  $J_{\text{P-H}} = 11.0$  Hz, 9 H, *PMe*<sub>3</sub>), 1.15 (d,  $J_{\text{P-H}} = 9$  Hz, 9 H, *PMe*<sub>3</sub>).  $^{31}\text{P}$  NMR (in THF at  $25^\circ\text{C}$ ):  $\delta$  227.42 (ddd,  $J_{\text{P-Rh}} = 105.69$  Hz,  $^2J_{\text{P-P}} = 219.17$  Hz,  $^2J_{\text{P-P}} = 19.30$  Hz, *PBu*<sub>2</sub>), 41.78 (d,  $^2J_{\text{P-P}} = 19.25$  Hz, *Fe-PMe*<sub>3</sub>),  $-16.09$  (dd,  $J_{\text{P-Rh}} = 136.15$  Hz,  $^2J_{\text{P-P}} = 219.12$  Hz, *Rh-PMe*<sub>3</sub>). Microanalysis: Calcd for  $\text{C}_{17}\text{H}_{36}\text{FeO}_4\text{P}_3\text{Rh}$ : C, 36.69; H, 6.47. Found: C, 37.20; H, 6.72.

From **2**: Carbon monoxide was bubbled through a THF (80 mL) solution of **2** (0.35 g, 0.57 mmol) at 1 atm. An immediate color change from red to yellow and the formation of a brown precipitate were observed. The solution was filtered and evaporated to dryness under vacuum. The residue was extracted with hexane ( $2 \times 20$  mL), filtered, and concentrated to ca. 10 mL. Cooling to  $-20^\circ\text{C}$  for 12 h gives **3** in about 35% yield.

**Chemical Reduction of 2 and 3. Isolation of  $[(\text{Me}_3\text{PO})\text{-Na}(15\text{-crown-5})]^+(\text{Co})_3\text{Fe}(\mu_2\text{-}t\text{-Bu}_2\text{P})\text{Rh}(\text{CO})(\text{PMe}_3)^-$ .** A solution of **3** (0.35 g, 0.62 mmol) in THF (30 mL) was added to an excess of sodium sand (5 g) and THF (40 mL) at room temperature. The suspension was stirred (4 h) during which time a gradual color change from yellow to red occurred. The mixture was filtered and 15-crown-5 (3 g) was added. The solution was stirred at room temperature (12 h) and then volatile materials were removed under vacuum. The residue was washed with hexane ( $3 \times 30$  mL) and extracted with diethyl ether (30 mL). Cooling ( $-20^\circ\text{C}$ ) produced yellow plates of **4** after ca. 1 week. They were collected and dried under vacuum. Yield 0.14 g (29%); mp  $90\text{--}92^\circ\text{C}$  dec. IR (KBr disk,  $25^\circ\text{C}$ ) 1914 (m), 1880 (s), 1828 (sh), 1810 (s)  $\text{cm}^{-1}$ .  $^1\text{H}$  NMR (in  $\text{C}_6\text{D}_6$ ,  $25^\circ\text{C}$ ):  $\delta$  3.41 (br,  $w^{1/2} = 30$  Hz, 20 H, crown ether), 1.79 (br d,  $^2J_{\text{P-H}} = 12.5$  Hz, 9 H, *PMe*<sub>3</sub>), 1.58 (br d,  $^3J_{\text{P-H}} = 7.0$  Hz, 18 H, *t*-Bu<sub>2</sub>P), 1.37 (br d,  $^2J_{\text{P-H}} = 16.5$  Hz, 9 H, *PMe*<sub>3</sub>).  $^{31}\text{P}$  NMR (in THF,  $25^\circ\text{C}$ ):  $\delta$  277.75 (dd,  $J_{\text{P-Rh}} = 112.17$  Hz,  $^2J_{\text{P-P}} = 190.91$  Hz,  $^2J_{\text{P-P}} = 190.91$  Hz, *PBu*<sub>2</sub>), 37.43 (s, *Me*<sub>3</sub>PO),  $-12.40$  (dd,  $J_{\text{P-Rh}} = 129.87$  Hz,  $^2J_{\text{P-P}} = 191.95$  Hz, *PMe*<sub>3</sub>). Rigorous exclusion of oxygen yields a red oil with a virtually identical  $^{31}\text{P}$  spectrum excluding the singlet due<sup>30</sup> to *Me*<sub>3</sub>PO; the ESP spectrum in THF gives a broad signal,  $g = 2.074$ . Microanalysis: Calcd for  $\text{C}_{28}\text{H}_{56}\text{FeNaO}_{10}\text{P}_3\text{Rh}$ : C, 40.63; H, 6.77. Found: C, 40.42; H, 6.65. A similar reaction with **2** also gave **4** in moderate yield (25%, based on **2**).

**X-ray Data Collection and Structure Determination. General:** Data for both complexes were collected on an Enraf-Nonius CAD-4 diffractometer with use of a graphite monochromated Mo  $K\alpha$  radiation. Data were collected by the  $\theta/2\theta$  scan technique at  $23 \pm 2^\circ\text{C}$ . All calculations were performed on a PDP 11/44 computer with the Enraf-Nonius software package "SDP-PLUS" (B. A. Frenz and Associates, College Station, Texas 77840, 4th ed., 1981).<sup>31</sup>

**2:** Crystals of **2** were grown from hexane solutions at  $-20^\circ\text{C}$  and mounted in thin-walled glass capillaries under nitrogen. Unit cell parameters were obtained from 25 carefully centered reflections ( $24^\circ < 2\theta < 26^\circ$ ).

Systematic absences ( $0k0$ ,  $k = 2n$ ) indicated a choice of the monoclinic space groups  $P2_1$  or  $P2_1/m$ .  $P2_1$  was chosen on the basis of successful refinement. Data were collected in the  $\pm h, +k, +l$  quadrant. Details of the crystal data parameters and other relevant information are collected in Table I. Data were corrected for Lorentz and polarization effects and for adsorbance with use of an empirical  $\Psi$  scan method (program EAC). An anisotropic decay correction was also made (3% decay of standard reflections). The structure was solved by direct methods (MULTAN)<sup>32</sup> followed by successive cycles of difference Fourier maps followed by least-squares refinement. A non-Poisson contribution

(30) The  $^{31}\text{P}$  resonance of *Et*<sub>3</sub>PO in solution is  $\delta$   $-48$  ppm, but complexation to the  $\text{Na}^+$  may move the resonance downfield. Emsley, J.; Hall, D. *The Chemistry of Phosphorus*; Harper and Row: New York, 1976; p 82.

(31) *SDP Plus*, 4th ed.; B. A. Frenz and Associates: College Station, Texas, 1981.

(32) Germain, G.; Main, P.; Wolfson, M. M. *Acta Crystallogr., Sect. A Cryst. Phys. Diffr. Theor. Gen. Crystallogr.* **1971**, *A27*, 368.

(29) Bard, A. J.; Faulkner, L. R. *Electrochemical Methods*; Wiley: New York, p 701.

to the weighting scheme with an experimental instability factor,  $P$ , was used in the final stages of refinement ( $P = 0.06$ ).<sup>33</sup> Non-hydrogen atoms were refined anisotropically except for some carbon atoms that were refined isotropically (see Table IV). Hydrogen atoms were not located. The relatively high shift to error ratio is probably due to thermal motion in the *t*-Bu groups. The maximum peak in the final difference Fourier map was  $0.65 \text{ e}\text{\AA}^{-3}$  and it was located  $1.19 \text{ \AA}$  from C(20). Scattering factors were taken from ref 34. The correct absolute configuration for **2** was determined by anomalous dispersion techniques.

**4:** Crystals of **4** were grown from hexane solutions ( $-20 \text{ }^\circ\text{C}$ ) and mounted in thin-walled glass capillaries under nitrogen. Unit cell parameters were obtained by carefully centering 25 reflections having  $2\theta$  values between  $20.0^\circ$  and  $28.0^\circ$ . The monoclinic space group  $P2_1/c$  (No. 14) was uniquely determined by systematic absences ( $h0l, l = 2n + 1$ ;  $0k0, k = 2n + 1$ ). Data were collected in the  $+h, +k, \pm l$  quadrant. Details of the crystal data parameters and other relevant information are collected in Table I. The data were corrected for Lorentz and polariz-

ation effects. No absorption correction was made since none was deemed necessary. A 25% decay of the standard reflections occurred after 3500 reflections so a new crystal was mounted and data collection was resumed. This crystal also had a 25% decay of standards over the course of data collection and an anisotropic decay correction was applied. The observed structure factors of equivalent reflections were averaged. The structure was solved by direct methods (MULTAN) followed by successive cycles of difference Fourier maps followed by refinement. A non-Poisson contribution weighting scheme with  $P = 0.06$  was used in the final stages of refinement. The Rh, Fe, P, and Na atoms were refined anisotropically and the remaining atoms isotropically. Hydrogen atoms were not located. The maximum peak in the final difference Fourier map had a height of  $0.69 \text{ e}\text{\AA}^{-3}$  and was located  $1.15 \text{ \AA}$  from C(11).

**Acknowledgment.** We thank the National Science Foundation (Grants CHE 85-17759 and CHE84-02135), the Robert A. Welch Foundation (F-816), and the Texas Advanced Technology Research Program for support. R.A.J. thanks the Alfred P. Sloan Foundation for a fellowship (1985-1987).

**Supplementary Material Available:** Complete tables of bond lengths, angles, and thermal parameters for **2** and **4** and a view of the unit cell of **4** (10 pages); observed and calculated structure factor tables for **2** and **4** (34 pages). Ordering information is given on any current masthead page.

(33)  $P$  is used in the calculation of  $\sigma(I)$  to downweight intense reflections in the least-squares refinement. The function minimized was  $\sum \omega(|F_o| - |F_c|)^2$  where  $\omega = 4(F_o)^2 / [\sum (F_o)^2]^2$ , where  $[\sum (F_o)^2]^2 = [S^2(C + R^2B) + \{P - (F_o)^2\}^2] / Lp^2$ , where  $S$  is the scan rate,  $C$  is the total integrated peak count,  $R$  is the ratio of scan time to background counting time,  $B$  is the total background count, and  $Lp$  is the Lorentz-polarization factor.

(34) *International Tables for X-Ray Crystallography*; Kynoch: Birmingham, England, 1974; Vol. 4.

## Substituent Effects on $\eta^2$ -Coordinated Arene Complexes of Pentaammineosmium(II)

W. Dean Harman, Mikiya Sekine, and Henry Taube\*

Contribution from the Department of Chemistry, Stanford University, Stanford, California 94305. Received November 19, 1987

**Abstract:** Pentaammineosmium(II) reacts with substituted benzenes to yield complexes in which the arene is coordinated  $\eta^2$  to the osmium. The surprising stability of these complexes is attributed to the high tendency of this metal center to back-bond. Unlike cationic  $\eta^6$ -arene complexes, both electron-donating and -withdrawing substituents on the ring stabilize the Os(II) with respect to arene dissociation. By oxidizing these compounds electrochemically, the stabilities of the Os(III)-arene analogues have also been investigated. For these complexes in which the back-bonding interaction has been diminished, electron-withdrawing substituents are found to destabilize the complex. Also attributable to  $\pi$  back-bonding are the relatively slow rates of tautomerization found in the osmium(II)-arene species.

The chemistry of arenes with transition-metal centers has developed considerably over the last two decades.<sup>1a-c</sup> Though a wealth of complexes have been studied in which the metal coordinates  $\eta^6$  to the aromatic ligand, far less is known about the lower coordination modes. Recently, particular interest has been given to  $\eta^2$ -coordinated arenes because of their suspected role as intermediates in C-H activation,<sup>2a-e,33</sup> yet only a handful of these species have been isolated. Typically,  $\eta^2$ -arene complexes are unstable with respect to dissociation or deprotonation of the aromatic ligand. Their instability can in part be attributed to the loss of resonance energy experienced upon coordination.<sup>1d</sup>

Our interest in the reactivity of pentaammineosmium(II) with unsaturated ligands has recently led to the discovery of a stable  $\eta^2$  complex of benzene.<sup>3</sup> This species,  $[\text{Os}(\text{NH}_3)_5(\eta^2\text{-C}_6\text{H}_6)]^{2+}$

(**1**), is resistant to deprotonation, is stable as a triflate salt for months, and persists, even in aqueous solution, for many hours at room temperature. We felt pentaammineosmium(II) would lend itself nicely to a systematic study of this unusual mode of arene bonding, allowing us to explore the effect of a substituent on the coordination position and stability of the  $\pi$ -bound species. By exploitation of the facile one-electron oxidation of these materials, the study has been extended to  $\eta^2$ -coordinated arene complexes of Os(III) as well.

### Experimental Section

Reagents: TMB = 1,2,3,4-tetramethylbenzene; Otf =  $\text{CF}_3\text{SO}_3^-$ ; DMPP = 2,2-dimethylpropionophenone; DME = 1,2-dimethoxyethane; DMA = *N,N*-dimethylacetamide; TBB = *tert*-butylbenzene; NMP = *N*-methylpyrrolidinone; isn = isonicotinamide; py = pyridine.

Infrared spectra were recorded on an IBM 98 FTIR spectrometer and <sup>13</sup>C and <sup>1</sup>H NMR spectra on a Varian XL-400 spectrometer.<sup>4</sup> Electrochemical experiments were performed under argon with a PAR model 173 potentiostat driven by a PAR Model 175 universal programmer. Cyclic voltammograms were recorded from +1.0 to -1.5 V (NHE) with a Pt<sup>0</sup> working electrode (1 mm<sup>2</sup>), a Pt<sup>0</sup> counter electrode, and a reference cell consisting of a Au<sup>0</sup> button in a DME solution containing FeCp<sub>2</sub>

(1) (a) Silverthorn, W. E. *Adv. Organomet. Chem.* **1975**, *13*, 47. (b) Gastingier, R. G.; Klabunde, K. J. *Transition Met. Chem.* **1979**, *4*, 1. (c) Muetterties, E. L.; Bleeke, J. R.; Wucherer, E. J. *Chem. Rev.* **1982**, *82*, 499. (d) Brauer, D. J.; Krüger, C. *Inorg. Chem.* **1977**, *16*, 884.

(2) (a) Sweet, J. R.; Graham, W. A. G. *J. Am. Chem. Soc.* **1983**, *105*, 305. (b) Sweet, J. R.; Graham, W. A. G. *Organometallics* **1982**, *2*, 135. (c) Jones, W. D.; Feher, F. J. *J. Am. Chem. Soc.* **1982**, *104*, 4240. (d) Jones, W. D.; Feher, F. J. *J. Am. Chem. Soc.* **1984**, *106*, 1650. (e) Chatt, J.; Davidson, J. M. *J. Chem. Soc.* **1965**, 843.

(3) Harman, W. D.; Taube, H. *J. Am. Chem. Soc.* **1987**, *109*, 1883.

(4) All <sup>1</sup>H NMR spectra are presented in ppm shift from tetramethylsilane.